



# Arctic temperature and precipitation extremes in present-day and future storyline-based variable resolution Community Earth System Model simulations

René R. Wijngaard<sup>1</sup>, Willem Jan van de Berg<sup>1</sup>, Christiaan T. van Dalum<sup>1</sup>, Adam R. Herrington<sup>2</sup>, and Xavier J. Levine<sup>3</sup>

Correspondence: René R. Wijngaard (r.r.wijngaard@uu.nl)

**Abstract.** Over the last few decades, the Arctic region has warmed up at a greater rate than elsewhere on the globe, partly resulting from the on-going loss of sea ice and seasonal snow over land. It is projected that the amplified warming of the surface will continue in the future. In addition, the intensity and frequency of temperature and precipitation means and extremes are projected to change, which may pose serious threats for human infrastructure and livelihoods. To assess (future) climate extremes, advanced modelling approaches with (regionally) refined resolution could be helpful.

In this study, we use the variable-resolution Community Earth System Model version 2.2 (VR-CESM) to evaluate and assess present-day and future climate extremes, such as heat waves and heavy precipitation, over the Arctic. Applying a globally uniform 1° grid and a VR grid with regional grid refinements to 28 km over the Arctic and Antarctica, we run 30-year present-day (1985–2014), 10-year present-day (2005–2014), and future (2090–2099) simulations with interactive atmosphere and land surface models, and prescribed sea ice and sea surface temperatures. We use the 30-year simulation to evaluate the ability of the VR grid to simulate climate extremes by comparison with gridded outputs of the globally uniform 1° grid, reanalysis-based datasets, and a regional climate model. The 10-year simulations follow two storylines of Arctic climate change representing a combination of strong/weak Arctic tropospheric warming and strong/weak SST warming in the Barents-Kara Seas and are used to assess future climate extremes by focussing on temperature and precipitation extremes. The outcomes show that the VR grid generally performs better in simulating precipitation extremes, while the globally uniform 1° grid generally performs better in simulating temperature extremes. Future projections suggest that high temperature extremes will generally increase both in intensity and duration, whereas low temperature extremes will decrease in intensity and duration, especially over regions dominated by SST warming and large sea ice loss. Further, wet precipitation extremes are projected to increase in intensity and frequency. The outcomes of this study may contribute to an improved understanding on future climate extremes and its implications.

<sup>&</sup>lt;sup>1</sup>Institute for Marine and Atmosphere Research Utrecht, Utrecht, the Netherlands

<sup>&</sup>lt;sup>2</sup>Climate and Global Dynamics Laboratory, NSF National Center for Atmospheric Research, Boulder, CO, USA

<sup>&</sup>lt;sup>3</sup>NORCE Norwegian Research Centre, Bjerknes Centre for Climate Research, Bergen, Norway





## 1 Introduction

In recent decades, the Arctic region has warmed up at a greater rate than elsewhere on the globe, a phenomenon known as "Arctic amplification" (Rantanen et al., 2022). Although the exact causes are still under debate, numerous studies have shown that Arctic amplification is caused by several feedback mechanisms involving interactions between the atmosphere, ocean, sea ice, and land surface, such as enhanced ocean-atmosphere coupling and changing surface albedos resulting from the ongoing loss of sea ice and snow over land (Screen and Simmonds, 2010; Dai et al., 2019; Park et al., 2019; Previdi et al., 2021; Rantanen et al., 2022). Under increasingly warmer climate conditions, high temperature extremes, such as warm days/nights and heat waves, have become more frequent in recent decades, while low temperature extremes, such as cold days/nights and cold spells, have become less frequent (Matthes et al., 2015; Walsh et al., 2020). Only in winter have cold extremes become more frequent over parts of North America and Asia, most likely due to the warming-induced weakening of the polar vortex, leading to more frequent cold outbreaks (Kim et al., 2014; Kug et al., 2015; Matthes et al., 2015; Johnson et al., 2018). In contrast to temperature extremes, systematic trends for precipitation extremes have not been observed and are more regional in nature due to the greater spatial variability of precipitation, the lack of measurements at high latitudes and altitudes, the accuracy of measurements, and uncertainties associated with atmospheric reanalyses (Walsh et al., 2020). According to Walsh et al. (2020), increasing trends in precipitation extremes have been observed over much of the Arctic land area, although regionally decreasing trends or no trends have also been observed.

In the future, Arctic warming is projected to continue, altering the intensity and frequency of temperature extremes (Sillmann et al., 2013b; Screen et al., 2015; Landrum and Holland, 2020; Walsh et al., 2020). As warming continues, precipitation is expected to increase, generally in line with the Clausius-Clapeyron relationship, which describes an increase in atmospheric moisture content under warmer climate conditions (Pfahl et al., 2017). In addition, precipitation is expected to increasingly shift from snow to rain, and the intensity and frequency of wet (dry) precipitation extremes are projected to increase (decrease) (Sillmann et al., 2013b; Screen et al., 2015; Landrum and Holland, 2020; Walsh et al., 2020; Paik et al., 2023). The changing intensity and frequency of temperature and precipitation extremes could ultimately lead to more frequent floods, wildfires, and reduced agricultural production, with profound impacts on ecosystems, human infrastructure and livelihoods (Hirabayashi et al., 2013; Masrur et al., 2018; Walsh et al., 2020; Overland, 2022). Given the potential future impacts of temperature and precipitation extremes in the Arctic, there is a need to develop adaptation and mitigation strategies that can help reduce potential adverse impacts on vulnerable Arctic communities and ecosystems.

Developing future adaptation and mitigation strategies is a challenging task due to the wide range of climate change projections resulting from uncertainties in possible future greenhouse gas emission scenarios, incomplete understanding of physical processes and their representation in climate models, and natural variability within the climate system (Hawkins and Sutton, 2009; Overland et al., 2019; McCrystall et al., 2021; Levine et al., 2024). To strengthen decision-making processes related to the development of adaptation and mitigation strategies, a number of possible climate outcomes – storylines – can be investigated. Storylines can be described as a physically self-consistent unfolding of past events or a plausible future pathway representative for regional climate change (Shepherd et al., 2018). Storylines have been generated using two distinct methodologies accord-





ing to the goal they want to achieve. Event-based storylines use an extreme synoptic event and apply changes to the mean state of the atmosphere to quantify the resulting change in impacts (e.g., Sillmann et al., 2021; Chan et al., 2022). Dynamical storylines use a multi-variate linear regression to generate climate states based upon the dependence of those climate state to predetermined climate indices; those climate indices generally represent a well-known change in the atmospheric, oceanic or sea ice state (e.g., Zappa and Shepherd, 2017; Zappa, 2019; Mindlin et al., 2020; Williams et al., 2024). Recently, dynamical storylines for the Arctic have been developed by Levine et al. (2024) that describe future pathways for Arctic summer climate change. These storylines are based on two different drivers that explain substantial fractions of the surface climate response to global warming in the Arctic, namely: 1) warming of the Arctic lower troposphere and 2) warming of the sea surface in the Barents-Kara Sea. As both drivers are expected to lead to changes in the occurrence and intensity of temperature and precipitation extremes, the Arctic storylines could contribute to a better understanding of the possible range of impacts of regional climate change on the intensity and frequency of temperature and precipitation extremes over the Arctic.

To investigate present-day and future climate extremes in the Arctic, a variety of advanced modelling approaches have been used. Global climate models (GCMs) have often been used to assess the present-day state and future changes in temperature and precipitation extremes on a global scale (e.g., Sillmann et al., 2013b, a; Seneviratne and Hauser, 2020; Kim et al., 2020; Seneviratne et al., 2021). Although GCMs simulate temperature extremes and large-scale precipitation extremes reasonably well, high-resolution models ( $\Delta x = 0.25^{\circ}$  or higher) have shown the ability to simulate precipitation extremes better than coarser-gridded models (Wehner et al., 2014; O'Brien et al., 2016; Seneviratne et al., 2021). However, the use of high-resolution GCMs has been limited due to the large computational resources that are required to run these GCMs. In this context, regional climate models (RCMs) could be considered as a more suitable alternative. RCMs, such as those used in the Arctic-CORDEX experiment (https://climate-cryosphere.org/arctic-cordex/), can be run at a higher spatio-temporal resolution with horizontal grid spacings as fine as  $\sim$ 11 km, and are therefore able to better capture spatio-temporal variability in temperature and precipitation. In addition, RCMs are often more specialized than GCMs in the simulation of (polar) processes (e.g. the treatment of snow and ice) and more optimized for specific regions of interest. Nonetheless, RCMs need to be forced with GCMs or reanalysis products, which disables two-way interactions between the region of interest and the global domain and introduces inconsistencies in terms of model physics and dynamics between RCMs and GCMs.

To overcome the limitations associated with RCMs and the computational constraints associated with high-resolution GCMs, variable-resolution GCMs or Earth System Models (ESMs), such as the variable-resolution Community Earth System Model (VR-CESM), have been developed. VR-CESM (Zarzycki et al., 2014; Lauritzen et al., 2018) is a hybrid between regional and global climate models as it applies a regional grid refinement over a region of interest within a coarse-gridded global domain (Rhoades et al., 2016). VR-CESM has been used to study various processes in several regions. For example, with regional refinements up to 7 km, VR-CESM has been used to study regional climate, atmospheric rivers, glacier surface mass balance, and/or snowpack characteristics in the western USA (Rhoades et al., 2018), Chilean Andes (Bambach et al., 2021), Mediterranean (Boza et al., 2025), East Asia (Zhu et al., 2023), High Mountain Asia (Wijngaard et al., 2023), Greenland (van Kampenhout et al., 2019; Herrington et al., 2022; Loeb et al., 2024; Waling et al., 2024), and Antarctica (Datta et al., 2023). Furthermore, present-day and future climatic means and/or extremes have been assessed with VR-CESM over western





US, eastern China, and Greenland (Xu et al., 2022; Yin et al., 2024). However, assessments focusing on temperature and precipitation extremes over the entire Arctic region have not been conducted thus far.

The main objective of this study is to evaluate and assess present-day and future temperature and precipitation extremes over the Arctic, using VR-CESM. To this end, we apply a globally uniform 1° (~111 km) grid and a dual polar VR grid with horizontally refined grid spacings of 28 km (0.25°) over the Arctic and Antarctic with interactively coupled atmosphere and land surface models, and prescribed sea ice and sea surface temperatures. We run three different types of simulations with both model grids, namely: 1) present-day simulations covering a 30-year period (1985–2014), 2) present-day simulations covering a 10-year period (2005–2014), and 3) future simulations (2090–2099) following the high-emission SSP5-8.5 scenario. The 30-year present-day simulations are used to evaluate the performance of the VR-CESM grids through comparisons with grid-ded outputs from reanalysis datasets and a regional climate model. The 10-year present-day and future simulations are used to assess future changes in temperature and precipitation extremes by following two storylines of Arctic summer climate change representing a combination of strong/weak Arctic tropospheric warming and strong/weak SST warming in the Barents-Kara Seas. Compared to previous VR-CESM studies focusing on climate extremes and/or the Arctic, this study has several novelties. First, this study is the first VR-CESM application that evaluates and assesses present-day and future intensity and occurrence of temperature and precipitation extremes over the entire Arctic. Second, we use a storyline approach to assess future extremes over the Arctic, which can potentially improve decision-making processes related to the development of adaptation and mitigation strategies.

This paper is organized as follows. Section 2 briefly describes the model and highlights the methods and data. Section 3 presents and discusses the main outcomes of this study. Finally, Section 4 provides further discussion and the conclusions.

# 110 2 Data and Methods

## 2.1 Modelling setup

We used the Community Earth System Model version 2.2 (CESM2; Danabasoglu et al., 2020; Herrington et al., 2022), a state-of-the-art global Earth system model consisting of multiple model components (including atmosphere, oceans, land surface, rivers, sea ice and land ice) that can be run in a partially or fully coupled mode. In this study, we applied CESM in a partially coupled mode by interactively coupling prognostic atmosphere and land surface components, and using prescribed daily sea ice and sea surface temperatures to replace the active ocean and sea ice components. This model configuration follows the Atmospheric Model Intercomparison Project (AMIP) protocol (Gates et al., 1999).

The atmosphere component of CESM2, the Community Atmosphere Model version 6 (CAM6), is applied with a hydrostatic spectral element dynamical core that supports unstructured grids that eliminates polar singularities and enables VR capabilities (CAM6-SE; Zarzycki et al., 2014; Lauritzen et al., 2018; Gettelman et al., 2019). Physics parameterization schemes applied in CAM6 include the Cloud Layers Unified by Binormals (CLUBB) scheme simulating shallow convection, boundary layer turbulence, and cloud macrophysics (Bogenschutz et al., 2013); a deep convection scheme (Zhang and McFarlane, 1995); a two-moment cloud microphysics scheme with prognostic treatment of precipitation (MG2; Gettelman and Morrison, 2015);



130

140



the modal aerosol module (MAM4; Liu et al., 2016); a cloud-aerosol radiation scheme (Rapid Radiative Transfer Method for GCMs - RRTMG; Iacono et al., 2008); and anisotropic orographic gravity wave (Weimer et al., 2023) and form drag parameterization schemes (Beljaars et al., 2004). Our atmospheric model configuration uses a dry mass low-top vertical coordinate with a model top at  $\sim$ 40 km and 58 hybrid sigma-pressure levels in the vertical instead of the standard 32 levels of CESM2 (Lauritzen et al., 2018). The new enhanced vertical grid is planned for the CESM3 model and has a higher resolution in the planetary boundary layer and in the middle and upper troposphere, and is intended to improve the representation of moisture, temperature, and cloud profiles in the boundary layer and to reduce noise and spurious flow features (Skamarock et al., 2019; Huang et al., 2022).

CAM6 is coupled to the land surface component of CESM2, the Community Land Model version 5 (CLM5; Lawrence et al., 2019), which is applied with satellite vegetation phenology (CLM5-SP). CLM5 simulates the surface energy balance, hydrological processes, biogeochemical cycles, and their interactions with the atmosphere (Oleson et al., 2013). It includes several new and updated processes and parameterizations, such as for snow and surface discretization (Lawrence et al., 2019). Snow albedo and two-way radiative transfer in the snowpack are simulated with a snowpack radiative heating model (Snow, Ice, and Aerosol Radiative model – SNICAR; Flanner and Zender, 2005; Flanner et al., 2007). A multi-layer snow model with up to 12 layers of snow and a maximum allowed depth of 10 m water equivalent (w.e.) simulates important snow processes, such as melting and refreezing, and includes modifications for wind- and temperature-dependent fresh snow density and snow compaction (van Kampenhout et al., 2017). To represent the heterogeneity of the land surface, CLM5 uses a subdivision scheme that heterogeneously subdivides CLM5 grid cells into five different land units (natural vegetation, urban, lakes, crops, and glaciers), which can be further subdivided into soil/snow columns and patches representing plant functional types (PFTs) or crop functional types (CFTs) (Lawrence et al., 2019).

## 2.1.1 Grids and performance

The VR-CESM simulations performed in this study are run with two different spectral element grids: 1) a globally uniform 1° (~111 km) grid, hereafter referred to as NE30, and 2) a dual polar VR grid (Fig. 1), hereafter referred to as POLARRES. The POLARRES grid was generated by the SQuadGen software package (Ullrich, 2014). Partly based on the existing ARCTIC and ANTSI VR grids (Herrington et al., 2022; Datta et al., 2023), POLARRES has horizontal grid spacings of 0.25° (~28 km) over the Arctic and Antarctic (poleward of 60°N/S). Further, a transition grid with horizontal grid spacings of 0.5° (~55 km; poleward of 45°N/S) serves as a buffer between the Arctic and Antarctic domains and the global 1° (~111 km) domain. The total number of horizontal grid points on the POLARRES grid sums up to 186 194, which is about 3.8 times more than on the NE30 grid (48 600).

The topography of the VR-CESM grids was interpolated from an updated 30-arcsec global topography dataset comprising of the Global Multi-resolution Terrain Elevation Data (GMTED2010; Danielson and Gesch, 2011) of the United States Geological Survey (USGS) and the BedMachine topography (Morlighem et al., 2017, 2020), which includes terrain elevations of Greenland and Antarctica (Wijngaard et al., 2023). To interpolate the topography, we used the NSF-NCAR topography



165

185



generation software package (Lauritzen et al., 2015), which includes ridge finding (for the anisotropic orographic gravity wave scheme) and internal smoothing algorithms to improve the accuracy of high-resolution topography.

To ensure numerical stability, CAM physics (dynamics) time steps of 1800 s (300 s) and 450 s (75 s) were used for NE30 and POLARRES, respectively. Furthermore, hyperviscosity coefficients preventing numerical artefacts and instability are scaled according to the dimensions of a grid element, configured such that for each halving of the grid spacing the hyperviscosity coefficients decrease by about an order of magnitude (Guba et al., 2014; Zarzycki et al., 2014). The VR-CESM simulations were performed on the Cheyenne supercomputing facility at the NSF National Center for Atmospheric Research (NSF-NCAR; Computational and Laboratory, 2019). The computational cost of NE30 amount to about 5 300 core hours per simulated year (CHPSY), which is about 2 times more expensive than a globally uniform 1° SE grid applied with 32 vertical levels (2 500 CHPSY). The POLARRES grid has a computational cost of about 50 000 CHPSY, which is about 10 times more expensive than the NE30 grid. Using 1080-2520 processors (30-70 nodes), the throughput reached about 7 simulated years per wall-clock day for NE30 and about 0.6-1.2 simulated years per wall-clock day for POLARRES.

## 2.1.2 Parameter tunings

The regionally refined resolution associated with the POLARRES simulations most likely has an impact on the representation of clouds as found in previous studies performed with VR-CESM (Wijngaard et al., 2023; Boza et al., 2025). For this reason, we implemented additional parameter tunings (largely following Wijngaard et al. (2023)) for the POLARRES simulations to tune the low-level cloudiness, and the shortwave radiation and albedo over sea ice. First, we increased the strength of the damping for the 3rd moment of the vertical velocity in the large skewness regime (*clubb\_c11b*) from 0.35 to 0.375. Increasing the damping strength reduces the vertical velocity skewness of the cloud distribution and increases the fraction of low cloud cover (Guo et al., 2015; Boza et al., 2025). Second, to tune shortwave radiation and albedo over sea ice, we increased the snow grain radius (*r\_snw*) over sea ice from 1.25 to 1.5 standard deviations and decreased the snowmelt onset temperature (*dt\_melt*) over sea ice from 1.5 to 1.0 °C.

In addition, we implemented modifications to fix a model bug in the cloud microphysics (Shaw et al., 2022; Zhu et al., 2022). These modifications are largely based on the paleoclimate-calibrated CESM2 configuration of Zhu et al. (2022), which include a reduction of the microphysical timestep by increasing the number of microphysical substeps, and the removal of a limiter on the cloud ice number concentrations. For the NE30 simulations, we have adopted the number of microphysical substeps (micro\_mg\_num\_steps) from Zhu et al. (2022), which increases from 1 to 8 and corresponds to a microphysical timestep of 75s. For the POLARRES simulations, we maintained the microphysical timestep of 75s, corresponding to 3 microphysical substeps.

# 2.2 Experimental Design

To evaluate and assess present-day and future climate extremes, three different model experiments are run with and without regional grid refinement over the Arctic. First, we run present-day experiments for a 30-year period (1985–2014) while forcing VR-CESM with daily sea ice cover (SIC) and sea surface temperatures (SST) retrieved from the ERA5 reanalysis dataset



200

205

210



(Hersbach et al., 2020). These experiments (hereafter referred to as present-day A experiments) were used to evaluate the performance of the model grids in simulating present-day climate extremes and to understand the impact of regional grid refinement on the representation of climate extremes. Second, we run future storyline experiments for the period 2090–2099 using SST and SIC fields from CMIP6 models representing selected Arctic storylines that are physically plausible outcomes of Arctic summer climate change. The selected storylines follow the high-emission SSP5-8.5 scenario and were derived by Levine et al. (2024) based on two different climate drivers: 1) Arctic atmospheric warming at the 850 hPa level and 2) SST warming in the Barents-Kara Seas. In this study, we used two different Arctic storylines that show opposite paths of Arctic climate change, namely:

- 1. Storyline ST1 (corresponding to storyline B2 in Levine et al. (2024)): Strong Arctic tropospheric warming combined with weak SST warming in the Barents-Kara Seas (PolAmpl+BKSSTWarm-). Relative to the multi-model mean (MMM) climate change, this storyline is characterized by warmer and drier continents, weaker SST warming over the Arctic and North Atlantic Ocean (Fig. 2c), and reduced sea ice loss (Fig. 2g).
- 2. Storyline ST2 (corresponding to storyline B1 in Levine et al. (2024)): Weak Arctic tropospheric warming combined with strong SST warming in the Barents-Kara Seas (PolAmpl-BKSSTWarm+). Relative to the multi-model mean (MMM) climate change, this storyline is characterized by cooler and wetter continents, stronger SST warming (Fig. 2d), and stronger sea ice loss, especially in the Barents-Kara Seas (Fig. 2h).

Each storyline is represented by a CMIP6 model selected for its similarity to the storylines and its skill to simulate the historical climate. Here, the r1i1p1f1 member of the Norwegian Earth System Model version 2 (NorESM2-MM; Seland et al., 2020) and the r1i1p1f2 member of the CNRM-CERFACS Earth System Model version 2 (CNRM-ESM2-1; Séférian et al., 2019) model realizations represent storylines ST1 and ST2, respectively. Finally, we run another set of present-day experiments for a 10-year period (2005–2014) using SST and SIC fields from the same CMIP6 model realizations used for the future storyline experiments. These baseline experiments (hereafter referred to as present-day B experiments) are used (in combination with the future storyline experiments) to assess future changes in climate extremes over the Arctic. All model experiments were spun-up for a period of 1 year.

Greenhouse gas concentrations, tropospheric aerosols, and ozone concentrations are time-varying and prescribed in accordance with CMIP6 historical and SSP5-8.5 forcings for the present-day and future storyline experiments, respectively. Stratospheric aerosols were not prescribed for the model experiments in this study. The land surface distributions for the VR-CESM grids are partly transient and partly constant. The plant functional type (PFT) and crop functional type (CFT) distributions are transient and are interpolated from the Land Use Harmonization (LUH2) time series, which has been developed for CMIP6 (Hurtt et al., 2020). The LUH2 time series covers the period 1850-2100 and describes annual land changes based on the History Database of the Global Environment (HYDE version 3.2; Klein-Goldewijk et al., 2017) for present-day (1850–2015) and SSP-RCP-based Integrated Assessment Model (IAM) projections for the future (2015–2100). The distributions of other land surface classes, such as glaciers, lakes, and urban areas, are assumed to be constant in time and set to the distributions of the year 2000.



230

235

240



## 2.3 Model evaluation

To evaluate the performance of the NE30 and POLARRES grids in simulating the climatology and extremes of temperature and precipitation, we compared gridded outputs from the present-day A experiments (1985–2014) with gridded outputs from two different reanalysis products and an RCM. To this end, we used daily precipitation sums and daily maximum, minimum, and mean 2-meter temperature from ERA5 (reanalysis), JRA-3Q (reanalysis), and RACMO (RCM):

- The ERA5 reanalysis data (Hersbach et al., 2020) were retrieved from the KNMI Climate Explorer (https://climexp. knmi.nl/start.cgi; last access: 2 July 2024). Originally, the ERA5 reanalysis data are available on a ∼31 km grid and monthly or hourly intervals. However, the data retrieved from the KNMI Climate Explorer have been regridded to a spatial resolution of 0.5°x0.5° and are available at daily intervals.
- The Japanese Reanalysis for Three Quarters of a Century (JRA-3Q) reanalysis (Kosaka et al., 2024) is the successor of the JRA-55 reanalysis, which has recently been released by the Japanese Meteorological Agency. JRA-3Q reanalysis data have been retrieved from the Research Data Archive (RDA) of NSF-NCAR (https://rda.ucar.edu/datasets/ds640.0; last access: 12 August 2024) and are available on a TL479 grid (∼40 km).
- Regional Atmosphere Climate Model (RACMO) data are based on RACMO version 2.4, a recently updated RCM that
  is specially developed to simulate polar climate processes over Greenland, the Arctic, and Antarctica (van Dalum et al.,
  2024). RACMO is forced with SST, SIC, and multi-level ERA5 data of wind speed, temperature, humidity, and pressure,
  and is available on an 11 km grid.

All CESM output and reference data are regridded to a 1-degree finite volume grid (0.9°x1.25°), unless noted otherwise, to allow comparison between the CESM grids and reference data. Finally, we have not used the high-resolution CARRA (Copernicus Arctic Regional Reanalysis) reanalysis due to its limited domain coverage. The release of a new version of CARRA, covering the entire Arctic domain, is planned for 2025–2026 (CARRA, 2025).

# 245 2.4 Analysis of temperature and precipitation extremes

To evaluate and assess present-day and future temperature and precipitation extremes in the Arctic, we selected eight extreme metrics (Table 1), including four temperature extreme metrics and four precipitation extreme metrics. These metrics are analyzed using the Climate Data Operators (CDO) functions based on the European Climate Assessment (ECA) climate indices, which are consistent with the definitions of the Expert Team on Climate Change Detection and Indices (ETCCDI).

To analyze temperature extremes, we selected extreme metrics representing the intensity and duration of temperature extremes, where the annual maximum of daily maximum temperature (TXx) and the annual minimum of daily minimum temperature (TNn) are used to analyze changes in the intensity of temperature extremes. To analyze changes in the duration of temperature extremes, we used the Warm Spell Duration Index (WSDI) and Cold Spell Duration Index (CSDI) as proxies for heat waves and cold spells, respectively. Here, the warm (cold) spell duration index is defined as the annual number of days in



260

265



intervals of at least 6 consecutive days on which TX (TN) is higher (lower) than the 90<sup>th</sup> (10<sup>th</sup>) percentile of TX (TN). The 90<sup>th</sup> (10<sup>th</sup>) percentile of TX (TN) is calculated for each calendar day using a 15-day running window for the base periods (1985–2014 for present-day A and 2005–2014 for present-day B). To derive the future WSDI and CSDI metrics, we used the historical 90<sup>th</sup> (10<sup>th</sup>) percentile calculated for the present-day B base period as a threshold.

We assessed the intensity of precipitation extremes by analyzing the  $99^{th}$  percentile of daily precipitation sums (P99) and the highest 5-day precipitation sums (RX5day). We also analyzed the number of heavy precipitation days (R10mm; defined as daily precipitation equal to or greater than  $10 \, \mathrm{mm} \, \mathrm{d}^{-1}$ ) and the greatest number of consecutive dry days with daily precipitation less than  $1 \, \mathrm{mm} \, \mathrm{d}^{-1}$  (CDD) to assess the frequency of heavy precipitation days throughout the year and the longest duration of dry spells, respectively.

The climatology and extremes of temperature and precipitation are analyzed by using probability density functions (PDFs) and regional averages that are calculated for four different Arctic land regions, one ocean region and one sea ice region covering areas poleward of 60°N (Fig. 1). Arctic land regions are based on regional domains defined by Seneviratne et al. (2012), namely Alaska and Western Canada (AWC; 105-168°W; 60-75°N), Eastern Canada and Greenland (ECG; 10-105°W; 60-85°N), Scandinavia (SCA; 0-40°E; 60-85°N) and Siberia (SIB; 40-180°E; 60-85°N). The sea ice region (SIC) is based on the maximum extent of sea ice cover during the present-day A (1985–2014) or present-day B (2005–2014) periods, taking into account all grid cells with sea ice cover greater than 15%. The ocean region (OCN) includes all ocean grid cells poleward of 60°N that are not classified as sea ice. The PDFs are constructed by sampling temperature or precipitation for all grid points in a specific region, while regional averages are based on metrics that have been calculated for each grid point within the respective regions. To avoid the effects of polar singularities on PDFs, CESM output and reference data are regridded to the NE30 grid (to allow a uniform comparison between the CESM grids and reference data), prior to the construction of the PDFs.

#### 275 **3 Results**

280

## 3.1 Evaluation

# 3.1.1 Temperature Extremes

Before assessing future changes in temperature and precipitation extremes in the Arctic, we evaluate the performance of NE30 and POLARRES in representing temperature and precipitation climatology and extremes. Figure 3 shows the present-day A (1985–2014) annual mean near-surface temperature differences between the NE30 and POLARRES grids, and the gridded outputs of ERA5, JRA-3Q, and RACMO. Both NE30 and POLARRES show warm temperature biases over most of the land surface and cold biases over the central Arctic, Greenland, and northeastern Canada, where POLARRES is colder on average than NE30. Here, the cold biases relative to ERA5 are largest, with a mean bias of -1.06 °C and -1.51 °C for NE30 and POLARRES (Figs. 3a-b), respectively (i.e. calculated over a domain poleward of 60°N), followed by RACMO (-0.98 °C/-1.44 °C for NE30/POLARRES; Figs. 3e-f) and JRA-3Q (-0.27 °C/-0.73 °C for NE30/POLARRES; Figs. 3c-d).



290

295

300

305

315

320



The cold biases over the central Arctic, Greenland, and northeastern Canada are also visible in the present-day A annual temperature probability density functions (PDFs), as shown in Figure 4. The PDFs show that CESM is colder than ERA5 and RACMO over ECG and SIC and colder than JRA-3Q over SIC (Figs. 4b,f). In particular, in low temperature regimes (i.e., the lower tail) it is 2-5 °C colder in NE30/POLARRES than in ERA5, JRA-3Q, or RACMO, with temperatures below -30 °C occurring more frequently in CESM and temperatures between -30 °C and -10 °C occurring more frequently in ERA5, JRA-3Q, or RACMO. In other regions, the PDFs of CESM and the reference data are mostly similar, except for temperature regimes around 0°C, which tend to occur more frequently in CESM over the land regions (Figs. 4a-d).

To evaluate the performance of CESM in simulating temperature extremes and to better understand the patterns of the cold bias over the Arctic, we compare CESM output with ERA5. Figure 5 shows the differences between CESM and ERA5 for the present-day A temperature extreme metrics (TXx, WSDI, TNn, and CSDI). For the annual maximum temperature (TXx), NE30 and POLARRES show cold biases over northeastern Canada and to a lesser extent over the central Arctic (Figs. 5b-c), and warm biases over the continental mid-latitudes. In general, POLARRES shows small improvements in TXx (i.e., the bias decreases by 0.2 °C on average), especially over Siberia, Alaska, and Scandinavia (Fig. 5d). However, the cold bias is enhanced over northeastern Canada. For the warm spell duration index (WSDI), the biases between the CESM grids and ERA5 are mostly negative (Figs. 5f-g), with the biases becoming slightly more negative in POLARRES (Fig. 5h). Only a few positive biases (especially in NE30) are found over Scandinavia, Greenland, and the western Canada. The annual minimum temperature (TNn) is associated with larger biases than TXx, with warm biases over land and to a lesser extent over the oceans, and large cold biases over the central Arctic (Figs 5j-k). Here, the TNn bias is slightly more negative in POLARRES with decreasing TNn over most of the Arctic, especially over Greenland, Iceland, Scandinavia, Svalbard and the Barents-Kara Sea region (Fig. 51). The decrease in TNn may be partly due to better resolved topography. Cold spell duration index (CSDI) biases are generally negative over much of the central Arctic and Greenland in NE30 and over parts of Scandinavia in POLARRES (Figs. 5n-p), indicating a decrease in the number of cold spell days relative to ERA5. Considering that both the annual mean temperature and the daily minimum temperature (TN) show a cold bias relative to ERA5 (especially over the central Arctic and Greenland; Figs. 3 and S1f-h), the negative CSDI biases are rather counter-intuitive. A possible explanation for the opposite patterns is that the variability of the daily minimum temperature differs between ERA5 and CESM. For example, the variability of the daily minimum temperature over sea ice is lower in ERA5 than in CESM (not shown), which may be partly due to the fixed sea ice thickness in ERA5 (i.e., 1.5 m; Batrak and Müller, 2019). In CESM, however, the sea ice thickness is variable, which leads to a higher variability of the daily minimum temperature and thus a lower probability of meeting the cold spell criteria (Table 1), ultimately resulting in a lower number of cold spell days.

Comparisons between CESM output and other reference data (i.e., JRA-3Q and RACMO) (Figs. S2 and S3) show mostly similar patterns including cold TXx biases over northeastern Canada, cold TNn biases over the sea-ice-dominated regions, and warm TNn (TXx) biases over most of the land (continental mid-latitudes) (Figs. S2b-c,j-k and S3b-c,j-k). Spatially, the cold and warm TNn (TXx) biases correspond well to the patterns of the climatological biases (Fig. 3). However, the magnitude of the extreme temperature biases is much larger. One of the possible explanations for the cold biases are large warm near-surface temperature biases of 5-10°C over sea ice that can be found in reanalysis products, such as ERA5 and JRA-55 (the predecessor



330

335

350



of JRA-3Q), during winter clear sky conditions (Batrak and Müller, 2019; Zampieri et al., 2023). These warm biases are mainly due to the poor representation of the snow layer on top of the sea ice and the thickness of the sea ice itself (Batrak and Müller, 2019; Zampieri et al., 2023). The warm biases in reanalysis products can also to some extent explain the cold biases between CESM and RACMO as RACMO is forced with sea ice, SST, and multi-level data (temperature, wind, humidity, and pressure) from ERA5 and thus inherits ERA5 uncertainties. The uncertainties related to reanalysis products, such as ERA5, indicate that the cold biases in CESM could be exaggerated. To understand the magnitude of the cold bias, validation of near-surface temperature against observations from meteorological stations in the Arctic is recommended in future research.

Another possible explanation for the cold biases in CESM is a bias in the cloud forcing. For example, Herrington et al. (2022) found negative biases in the summer shortwave cloud forcing over much of the Arctic, suggesting excessive reflection and cooling. Similar negative biases were also found in NE30 and POLARRES over the Arctic land regions (Figs. S4a-c), especially over northeastern Canada. However, the biases in the summer shortwave cloud forcing cannot fully explain the enhanced cold bias over northeastern Canada in POLARRES. Although the summer shortwave cloud forcing bias becomes more positive in POLARRES, the near-surface temperature still shows a cooling response relative to NE30, which is possibly due to the increase in summer surface albedo over northeastern Canada and the central Arctic (Figs. S4d-f). Here, the increased summer surface albedo could be related to the increased snow depth over northeastern Canada during that season (not shown). Finally, the warm bias over land in CESM is most likely related to a precipitation deficit, which leads to a soil moisture deficit and ultimately less evaporative cooling and higher temperatures (Boza et al., 2025; Lin et al., 2017; Lorenz et al., 2016).

# 3.1.2 Precipitation Extremes

Figure 6 shows the present-day A annual mean precipitation differences between the NE30 and POLARRES grids, and the gridded outputs from ERA5, JRA-3Q, and RACMO. Compared to ERA5, JRA-3Q, or RACMO, CESM generally tends to be wetter over the ocean and most of the Arctic land regions (i.e., poleward of 60°), and drier over most of the continental midlatitudes, which supports the existence of a precipitation deficit that contributes to the warm near-surface temperature biases over the continental mid-latitudes (Figs. 3 and 5). On average, CESM is wetter than ERA5, JRA-3Q, or RACMO with mean biases ranging from 0.02-0.07 mm d<sup>-1</sup> in NE30 (Figs. 6a,c,e) to 0.01-0.06 mm d<sup>-1</sup> in POLARRES (Figs. 6b,d,e), with the smallest biases relative to RACMO (Figs. 6e-f), followed by JRA-3Q (Figs. 6c-d) and ERA5 (Figs. 6a-b). Although POLARRES generally tends to be slightly drier than NE30, the precipitation rates are higher over elevated terrain, such as the mountainous terrains of Scandinavia, southern Iceland, and southern Alaska, mainly due to the better resolved topography.

Figure 7 shows the present-day A annual precipitation PDFs, which have been constructed on a NE30 grid to allow uniform comparison between the CESM grids and the reference data (also see Section 2.4). Extreme precipitation rates are generally lowest in NE30 and highest in RACMO, particularly over AWC, ECG, SCA, and SIC (Figs. 7a-c,f). POLARRES, JRA-3Q and ERA5 often show similar extreme precipitation rates. Only over SIB, ERA5 and JRA-3Q show lower extreme precipitation rates than NE30, POLARRES and RACMO (Fig. 7d). A possible explanation for the lower extreme precipitation rates in ERA5 and JRA-3Q is that extreme precipitation rates are underestimated as for example is found for ERA5 in Siberia (Clelland et al., 2024). Over OCN, the spread between CESM output and reference data is relatively small compared to the spread in other



360

365

370

380

385



regions (Fig. 7e). The differences between extreme precipitation rates found in CESM output and reference data can primarily be explained by differences in horizontal resolution, which is lowest for NE30 (~111 km), similar for POLARRES (~28 km), JRA-3Q (~40 km) and ERA5 (~31 km), and highest for RACMO (11 km).

To better understand the patterns of precipitation extremes over the Arctic, we compare the CESM output with ERA5. Figure 8 shows the differences between CESM and ERA5 for the present-day A precipitation extreme metrics (P99, RX5day, R10mm, and CDD). Compared to ERA5, the  $99^{th}$  percentile of precipitation (P99) over the continents is lower in NE30, especially over the mountainous regions along the eastern Pacific, Scandinavia, and southeastern Greenland and Iceland (Fig. 8b). In POLARRES, P99 increases over the same regions, but especially on the windward side of the mountainous regions, while P99 decreases on the more inland or leeward side, which is especially visible along the eastern Pacific and over southeastern Greenland (Figs. 8c-d). The highest 5-day precipitation sum (RX5day) biases are mostly positive in NE30 (Fig. 8f). Dry biases are present over only a few regions, including western Canada, the northern Atlantic, Europe, and western Russia. In POLARRES, dry biases decrease, and wet biases increase, especially at lower latitudes over East Asia and North America (Figs. 8g-h). The larger biases in POLARRES could be the result of a higher frequency and intensity of (extra-tropical) storm systems, which bring significant amounts of precipitation over a period of several days (Zarzycki and Jablonowski, 2014; Xu et al., 2022; Zhu et al., 2023). The number of heavy precipitation days (R10mm) shows positive biases over the oceans and negative biases over land in NE30, especially over mountainous regions along the eastern Pacific, southeastern Greenland and Iceland, Scandinavia, and Scotland (Fig. 8j). In POLARRES, positive biases decrease over the North Atlantic (Figs. 8k-1). Furthermore, there is a strong increase in heavy precipitation days over southeastern Iceland, Scandinavia, Scotland, and the eastern Pacific, and a decrease over the more inland or leeward sides of mountainous regions in southeastern Greenland, Scandinavia, and the eastern Pacific. Finally, the greatest number of consecutive dry days (CDD) shows a negative bias over the central Arctic in NE30 and POLARRES, which could indicate a more variable precipitation climatology in CESM, reducing the length of dry periods (Figs. 8n-o). Relative to NE30, CDD decreases slightly in POLARRES, except for a few areas in the Canadian Arctic and East Asia that show an increase in CDD (Fig. 8p).

Comparisons between CESM output and other reference data (JRA-3Q and RACMO; Figs. S5 and S6) show that the spatial patterns are mostly similar compared to the differences between NE30/POLARRES and ERA5. Compared to JRA-3Q, CESM grids show a similar performance compared to ERA5, although CESM tends to be slightly drier. Compared to RACMO, the biases are generally much more negative, indicating that precipitation in RACMO is more extreme in intensity and frequency, which is consistent with the larger extreme precipitation rates shown in Figure 7. The differences in extreme precipitation rates and metrics are primarily related to the different horizontal resolutions, with higher resolution grids generally simulating larger extreme precipitation rates and metrics, which is consistent with other studies showing the effect of horizontal resolution on (extreme) precipitation (Herrington et al., 2022; Bacmeister et al., 2014; Huang et al., 2022; Xu et al., 2022), and to some extent to different physics and parameterizations. The higher agreement between POLARRES and JRA-3Q and ERA5 suggests that POLARRES can better represent extreme precipitation than NE30. However, the discrepancies between POLARRES and RACMO also suggest to some extent that higher resolution grids are needed to further improve the representation of extreme



395

400



precipitation, which is also demonstrated by CESM simulations on (storm-resolving) grids with a horizontal resolution of 14 km or higher (Huang et al., 2022; Xu et al., 2022).

## 3.2 Future projections

# 3.2.1 Temperature Extremes

Towards the end of the  $21^{st}$  century mean temperature and temperature extremes are projected to increase in magnitude in both storylines. Figure 9 shows the present-day B (2005–2014) annual mean near-surface temperature and the projected future (2090–2099) changes in annual mean near-surface temperature for two different storylines and CESM grids (NE30 and POLARRES), and the differences between the grids. The present-day panels (Figs. 9a,c,e,g) show that the annual mean temperature is relatively similar for storyline ST1 (associated with strong Arctic tropospheric warming) and storyline ST2 (associated with strong SST warming in the Barents-Kara Seas), with ST1 being slightly colder than ST2 over the central Arctic. In addition, the present-day B annual mean temperature is slightly lower than the present-day A annual mean temperature over the central Arctic (not shown), due to the lower SST originating from CMIP6 models that represent the storylines (NorESM2-MM for ST1 and CNRM-ESM2-1 for ST2) and force CESM.

Present-day differences between POLARRES and NE30 (Figs. 9i,k) indicate that POLARRES is generally colder than NE30, except over Greenland and parts of Alaska and eastern Siberia, where POLARRES is warmer than NE30. These differences are partly related to the better resolved topography, especially over Alaska, Greenland, Iceland, Scandinavia and parts of Siberia. Towards the end of the century, both storylines show an increase in temperature (Figs. 9b,d,f,h). Here, ST2 can be characterized by a warmer Arctic in the future with temperature increases up to about 19 °C over the Barents-Kara Seas (Figs. 9d,h), which can be linked to the strong SST warming over the respective region (Fig. 2d). ST1 shows locally a temperature decrease (up to about 2-3 °C) over the northern Atlantic (Figs. 9b,f), due to SST cooling anomalies over the respective region (Fig. 2c). These SST cooling anomalies are most likely related to increased freshwater inflow and associated weakening of the Atlantic Meridional Overturning Circulation (AMOC) (Liu et al., 2020; Weijer et al., 2020). Future differences between POLARRES and NE30 (Figs. 9j,l) are relatively small for both storylines with mixed signals in ST1 and a slightly colder trend in POLARRES in ST2, especially over the North American continent.

Stronger ST2 temperature responses are also evident from the projected changes in regional temperature extremes as shown in Figure 10. In all regions, TXx and TNn are projected to increase, with the projected changes in high (low) temperature extremes (TXx (TNn)) being smaller (larger) than the projected changes in annual mean near-surface temperature (Figs. 10a-b). In addition, the ST2 increases are much larger than the ST1 increases, with differences of up to 11°C for TNn between ST1 and ST2 (Figs. 10a-b). Specifically over SIC, NE30 (POLARRES) projects temperature increases of up to 11°C (11°C) and 21°C (19°C) for TXx and TNn, respectively, suggesting that SST warming and associated sea ice loss have the strongest response on temperature over the sea ice itself. Temperature increases over land are generally smaller with increases in the range 3-9°C (7-10°C) and 6-12 °C (11-15°C) for TXx and TNn respectively in ST1 (ST2). Here, POLARRES predicts larger (smaller) temperature increases than NE30 for TXx (TNn), with more pronounced TXx differences over ECG in ST1



425

430

435

440

445

450



and over SCA in ST1 and ST2. The differences over ECG are associated with stronger warming over northeastern Canada in POLARRES (Fig. S7b), mostly due to large decreases in snow depth over the respective region (not shown). As the present-day snow depth is overestimated, this warming trend is likely to be spurious. The differences over SCA are mostly related to the stronger warming over the Eurasian continent (Fig. S7d). Temperature increases over the ocean are relatively small compared to the changes over land and sea ice, especially for ST1, which is most likely influenced by the projected cooling over the northern Atlantic (Figs. S8b,j and S9b,j).

Consistent with the expected temperature increases, the WSDI also increases, especially under ST2 and over SIC, and the CSDI decreases in all regions (Note that we have derived the future WSDI and CSDI metrics based on the present-day B percentile thresholds; see Section 2.4). The smaller ST1 WSDI (CSDI) increase (decrease) over OCN and to some extent over SCA (for WSDI only) is related to the projected cooling-induced decrease (increase) in WSDI (CSDI) in the northern Atlantic (Figs. S8f,n and S9f,n). The differences between POLARRES and NE30 are relatively small for the WSDI, although locally the differences are larger, e.g. over northeastern Canada (Figs. S7f,h), where POLARRES projects a higher WSDI. For the CSDI, the differences are generally less negative, consistent with the smaller TNn increases in POLARRES (Fig. 10b). The projected increases (decreases) in WSDI (CSDI) are consistent with the findings of Screen et al. (2015), who assessed future changes in regional climate extremes arising from Arctic sea ice loss, using regions similar to those used in this study. Although the magnitude of change in CSDI is similar to that found in Screen et al. (2015), the projected changes in WSDI are much larger in this study. For example, in ECG the projected increase in WSDI in the Screen et al. (2015) study is up to about 35 dyr<sup>-1</sup>, while in this study the projected increases are up to about 220 dyr<sup>-1</sup>. A possible explanation for these differences is that the future experiments performed in Screen et al. (2015) were based on "idealized" model experiments using prescribed present-day SST and future sea ice concentrations, whereas our experiments use both prescribed future SST and sea ice concentrations. This indicates that not only sea ice loss but also SST warming is an important driver of future changes in temperature extremes.

# 3.2.2 Precipitation Extremes

Figure 11 shows the present-day B (2005–2014) annual mean precipitation and projected future (2090–2099) changes in annual mean precipitation for two different storylines and CESM grids, and the differences between the grids. The present-day annual precipitation is similar for both ST1 and ST2 (Figs. 11a,c,e,g). However, regionally the annual mean precipitation is larger (smaller) in POLARRES, especially on the windward (leeward or more inland) sides of mountainous areas in the eastern Pacific/southern Alaska, southeastern Greenland, Iceland, and Scandinavia (Figs. 11i,k). In the future, both NE30 and POLARRES project an increase in annual precipitation over most of the Arctic in both storylines, with the exception of the north(east)ern Atlantic where precipitation is projected to decrease (Figs. 11b,f,d,h). These decreases are larger in ST1 and are associated with decreases in SST and near-surface temperature over the region (Figs. 2c-d and 9b,f,d,h). As the projected cooling is greater in ST1, the amount of atmospheric moisture available for precipitation (as depicted by the Clausius-Clapeyron relationship) is less and can therefore explain the greater precipitation decreases in ST1. Future differences between POLARRES and NE30 (Figs. 11j,l) show consistent regional patterns in both storylines with wetter trends in POLARRES over



460

465

475

480



the northern Atlantic, the Scandinavian mountain ranges, and the eastern Pacific coast, and drier trends over Greenland and some parts of the land (e.g. eastern Siberia in ST1 and Alaska in ST2).

Figure 12 shows the projected changes in regional precipitation extremes for two different storylines and CESM grids. In ST1 (ST2), P99, RX5day, and R10mm increase on average by  $\sim 3.0 \,(\sim 4.0) \,\mathrm{mm}\,\mathrm{d}^{-1}$ ,  $\sim 10$ -12 ( $\sim 15$ -18) mm, and  $\sim 4.0 \,(\sim 5.0) \,\mathrm{d}$ , respectively (Figs. 12a-c). These increases correspond to mean relative increases of 26-27% (30-32%), 32-35% (44-45%), and 49-52% (56-58%) for P99, RX5day, and R10mm, respectively (Figs S10b-d), indicating that the R10mm changes are relatively the largest. As the annual mean precipitation increases by  $\sim 0.3~\mathrm{mm\,d^{-1}}$  (21-22%) in ST1 and  $\sim 0.4~\mathrm{mm\,d^{-1}}$  (24-28%) in ST2 (Figs. 11b,f,d,h; Fig. S10a), the projected changes in the extremes are larger than the changes in the means. Regionally, the ST2 increases are often larger than the ST1 increases. Only over AWC the ST2 increases are slightly smaller than the ST1 increases for P99 and R10mm. The larger increases in ST2 are most likely related to the larger temperature increases in ST2, which lead to an increase in atmospheric moisture and thus more precipitation. Consistent with the increase in mean and extreme precipitation, the CDD shows a decrease in most regions, except for SCA and AWC (Fig. 12d). Over AWC, the POLARRES grid projects an increase in CDD in ST2, while over SCA the increase in CDD is more pronounced in ST2 (both NE30 and POLARRES) and to a lesser extent in ST1 (POLARRES only). Similar CDD increases over SCA were also found by Screen et al. (2015). The regions where CDD is projected to increase are characterized by a lower present-day CDD, which is found over most of the Arctic. In regions with high present-day CDD (central Arctic, north(east)ern Greenland and Canada, and eastern Siberia; Figs. S11m-p, S12m-p), CDD is projected to decrease. This means relatively dry regions will become wetter, while wetter regions will become wetter and experience longer periods of drought.

Regarding the differences between NE30 and POLARRES for future precipitation (extremes), the differences often show mixed signals depending on the extreme metric and the region, although for some regions and extreme metrics the differences are more pronounced. For example, over SCA, POLARRES predicts larger absolute increases in P99, RX5day, and R10mm for both storylines (Figs. 12 and S13). Furthermore, the RX5day differences are more pronounced over AWC, SIB, and SIC, where POLARRES predicts larger absolute increases. The larger RX5day increases could be related to the higher frequency and intensity of storm systems associated with higher resolution grids, as discussed above (Fig. 8). The larger increases over SCA can be explained by increased moisture fluxes and enhanced moisture convergence associated with grid refinement, as seen in Figure 13. This figure shows the future changes in the annual mean vertically integrated moisture flux convergence, and the 850 hPa zonal wind and moisture fluxes for ST1/ST2 and NE30/POLARRES, and the differences between NE30 and POLARRES. Both NE30 and POLARRES predict a strengthening of westerly moisture transport over most of the higher midlatitudes (i.e. roughly between 50°N and 70°N) in ST1 and over North America, northern Atlantic, and Europe in ST2 (Figs. 13a-c,g-i and S14). The NE30 moisture flux anomalies are associated with an eastward shift of the low-level North Atlantic jet in ST1 (Fig. 13d). The eastward shift of the North Atlantic jet also occurs in POLARRES but is accompanied by enhanced zonal wind near the climatological maximum of the jet (Figs. 13e-f). Here, the zonal wind changes are mainly due to changes occurring during winter (Figs. S15d-f and S16d-f). In ST2, the projected changes in zonal wind are much weaker compared to the ST1 changes, where NE30 does not show significant changes in the zonal wind over the northern Atlantic region (Fig. 13j). However, POLARRES predicts a poleward shift of the jet and a significant intensification of zonal wind between Iceland





and Scandinavia in ST2 (Fig. 13k). These changes can be associated with zonal wind changes that mainly occur during winter and to a lesser extent during summer (Figs. S15j-l and S16j-l). The zonal wind changes over the northern Atlantic are most likely driven by SST changes and to a lesser extent by sea ice loss (Smirnov et al., 2015; Köhler et al., 2024; Wills et al., 2024), although the mechanisms for the differences between ST1 and ST2 as well as the relative contributions of SST and sea ice changes are unknown and therefore require more research in the future. Finally, the enhanced westerly moisture transport in ST1 and ST2 is accompanied by enhanced moisture convergence along the Scandinavian mountain ranges and is indicative of an intensification of precipitation over the respective region (Fig. 13b-c,e-f), which can therefore explain why precipitation differences between NE30 and POLARRES are more pronounced over SCA and less pronounced in other regions. However, it is likely that other drivers (e.g. orographic-induced updrafts and convection) also play a role in the precipitation differences between NE30 and POLARRES. To understand the changes in the drivers of precipitation means and extremes with grid refinement under different SST and sea ice regimes more research is needed as well.

## 4 Discussion and Conclusions

505

515

520

We have evaluated and assessed present-day and future temperature and precipitation extremes over the Arctic, using the variable-resolution Community Earth System Model version 2.2 (VR-CESM). We applied a globally uniform 1° CESM grid (NE30) and a dual-polar VR grid with regional grid refinements to 28 km over the Arctic and Antarctica (POLARRES). Using both model grids, we run three different types of simulations with interactively coupled atmosphere and land surface models, and prescribed sea ice and sea surface temperatures, namely: a 30-year simulation (1985–2014) used to evaluate the model grids, and 10-year present-day (2005–2014) and future (2090–2099) simulations used to assess future changes in temperature and precipitation extremes. Here, the 10-year present-day and future simulations follow two storylines of Arctic summer climate change representing a combination of strong/weak Arctic atmospheric warming at the 850 hPa level and strong/weak SST warming in the Barents-Kara Seas. To evaluate and assess present-day and future temperature and precipitation extremes, we analyzed eight extreme metrics, including four extreme metrics each for temperature and precipitation.

The evaluations show that both NE30 and POLARRES have climatological warm temperature biases over most of the land surface and climatological cold temperature biases over the central Arctic, Greenland, and northeastern Canada, with cold biases being larger in POLARRES than in NE30. For temperature extreme metrics, POLARRES performs slightly better in simulating TXx, while NE30 performs better for other temperature extreme metrics (TNn, WSDI, and CSDI). Spatially, the cold and warm biases in TNn and TXx correspond well to the spatial patterns of the climatological biases, but the magnitude of the extreme temperature biases is much larger. The cold biases can be partly explained by large warm near-surface temperature biases in the reanalysis products, caused by poor representation of snow over sea ice and the thickness of the sea ice itself. In addition, the cold biases may be related to increased cloud cover (relative to the reference data) leading to excessive reflection and cooling, and increased summer surface albedo and snow depth over northeastern Canada and the central Arctic in POLARRES. However, to understand the magnitude of the cold bias in CESM, validation of near-surface temperature against meteorological observations in the Arctic is needed and thus recommended for future research.



525

530

535

540

545

550

555



NE30 and POLARRES have climatological dry biases over the continent and climatological wet biases over the oceans. The dry biases indicate a precipitation deficit over land, which may contribute to the warm biases over the land surface via a soil moisture deficit and associated reduced evaporative cooling. POLARRES performs slightly better than NE30 in simulating the precipitation climatology, with higher precipitation rates over mountainous terrain in Scandinavia, southeastern Greenland, and Alaska, which is mainly due to the higher grid resolution and better resolved topography. With respect to precipitation extremes, the performance of POLARRES and NE30 depends on the performance criteria (i.e. RMSE or bias) and the data used as reference (ERA5, JRA-3Q or RACMO) for the evaluation. Using the RSME as the performance criterion, POLARRES generally performs better than NE30 in simulating P99, R10mm, and CDD, while NE30 performs better in simulating RX5day. The larger RX5day biases in POLARRES could be related to a higher frequency and intensity of storm systems bringing significant amounts of precipitation over a period of several days.

Future projections suggest that annual mean temperature, TXx, TNn, and WSDI (CSDI) will mostly increase (decrease) in magnitude or duration in all regions of the Arctic, with the rate of change varying by region and the applied storyline. The projected increases are larger for ST2, with the largest increases being projected over the currently sea ice-dominated central Arctic. The larger increases in ST2 suggest that SST warming and associated sea ice loss over the Arctic have a stronger response than Arctic low-level tropospheric warming, especially over the sea ice itself. In ST1, increases in temperature extremes are especially smaller over the ocean and Scandinavia, and are accompanied by a local decrease in annual mean temperature due to projected cooling anomalies over the North Atlantic. Regarding the differences in projected changes by NE30 and PO-LARRES, the differences are more pronounced for TXx with larger increases in POLARRES over northeastern Canada and Greenland in ST1, which is mainly due to reduced snow depth over northeastern Canada, and over Scandinavia in ST1 and ST2, which is mainly due to stronger warming over the Eurasian continent.

Precipitation means and extremes are mostly projected to increase in intensity and frequency, with the projected changes in extremes being greater than the projected changes in mean precipitation. Only over the northern Atlantic, annual mean precipitation is projected to decrease due to local cooling-induced decreases in atmospheric moisture and precipitation. The projected changes are mostly stronger for ST2, which can be associated with the stronger warming-induced increases in atmospheric moisture and precipitation. The projected changes in CDD suggest that regions with high present-day CDD (e.g., central Arctic, north(east)ern Greenland and Canada, and eastern Siberia) will become wetter (i.e., CDD will decrease), and regions with low present-day CDD (e.g., Scandinavia) will experience longer periods of droughts (i.e., CDD will increase). Regarding the differences in regional projected changes by NE30 and POLARRES, the differences often show mixed signals depending on the extreme metrics and region but are especially more pronounced over Scandinavia as well as for RX5day. Here, POLARRES projects larger RX5day increases, which is due to the higher frequency and intensity of storm systems associated with higher resolution grids. Further, POLARRES projects larger increases in P99, RX5day, and R10mm, which is most likely due to enhanced westerly moisture transport and convergence over the respective region.

This study shows that, relative to the used reference data, VR-CESM generally outperforms a coarse-resolution CESM grid in simulating precipitation climatology and extremes, while a coarse-resolution CESM grid often outperforms VR-CESM in simulating temperature climatology and extremes. This implies that VR-CESM can be a useful modelling tool for simulating



560

565

580



present-day and future extremes in the Arctic, but also that model improvements are needed to reduce temperature biases. Additionally, more research is needed to improve our understanding on the drivers and mechanisms for warming-induced or grid refinement-induced changes in Arctic temperature and precipitation means and extremes.

Finally, this study demonstrates the large range that can exist between the projected changes in temperature and precipitation extremes of two different storylines. Nonetheless, the projected range in model outcomes is most likely smaller than the projected range of model outcomes that stem from CMIP6 scenario-based multi-model approaches. For example, the 5%-95% range of surface temperature changes as projected by CMIP6 models in the Arctic is about 9 °C under SSP5-8.5 (Lee et al., 2021), while the average range of near-surface temperature changes between ST1 and ST2 is about 2.5-3 °C in the Arctic at the end of the 21<sup>st</sup> century. This narrows down the uncertainty range, which means that the outcomes of this study, besides contributing to a better understanding of future temperature and precipitation extremes in the Arctic, could also be more helpful in the development of adaptation and mitigation strategies that cope with the adverse impacts of temperature and precipitation extremes.

570 Data availability. Publicly available data will be stored in a data archive on Zenodo (https://doi.org/10.5281/zenodo.14961708) upon publication. The data archive contains the daily near-surface temperature and precipitation output and calculated temperature and precipitation extreme metrics.

Author contributions. RRW and WJB designed the study. RRW ran the model with technical support of ARH. XJL developed the Arctic storylines. CTD provided the RACMO data used for evaluation of the model output. RRW analyzed the model results and prepared the text
 and figures. WJB supervised RRW. All authors contributed to the final text.

Competing interests. The contact author has declared that none of the authors has any competing interests.

Acknowledgements. We acknowledge the support of PolarRES (grant no. 101003590), a project of the European Union's Horizon 2020 research and innovation programme. Adam R. Herrington has been supported by the NSF National Center for Atmospheric Research, which is a major facility sponsored by the National Science Foundation (grant no. 1852977). Computing and data storage resources, including the Cheyenne supercomputer (https://doi.org/10.5065/D6RX99HX, Computational and Information Systems Laboratory, 2019), were provided by the Computational and Information Systems Laboratory (CISL) at NSF NCAR.





#### References

- Bacmeister, J. T., Wehner, M. F., Neale, R. B., Gettelman, A., Hannay, C., Lauritzen, P. H., Caron, J. M., and Truesdale, J. E.: Exploratory high-resolution climate simulations using the community atmosphere model (CAM), Journal of Climate, 27, https://doi.org/10.1175/JCLI-D-13-00387.1, 2014.
  - Bambach, N. E., Rhoades, A. M., Hatchett, B. J., Jones, A. D., Ullrich, P. A., and Zarzycki, C. M.: Projecting climate change in South America using variable-resolution Community Earth System Model: An application to Chile, International Journal of Climatology, https://doi.org/10.1002/joc.7379, 2021.
- Batrak, Y. and Müller, M.: On the warm bias in atmospheric reanalyses induced by the missing snow over Arctic sea-ice, Nature Communications, 10, https://doi.org/10.1038/s41467-019-11975-3, 2019.
  - Beljaars, A. C., Brown, A. R., and Wood, N.: A new parametrization of turbulent orographic form drag, Quarterly Journal of the Royal Meteorological Society, 130, https://doi.org/10.1256/qj.03.73, 2004.
  - Bogenschutz, P. A., Gettelman, A., Morrison, H., Larson, V. E., Craig, C., and Schanen, D. P.: Higher-order turbulence closure and its impact on climate simulations in the community atmosphere model, Journal of Climate, 26, https://doi.org/10.1175/JCLI-D-13-00075.1, 2013.
  - Boza, B., Herrington, A., Ilicak, M., Danabasoglu, G., and Sen, O. L.: Exploring Climate of the Euro-Mediterranean Using a Variable-Resolution Configuration of the Global Community Earth System Model (VR-CESM), Journal of Geophysical Research: Atmospheres, 130, https://doi.org/10.1029/2024JD041300, 2025.
  - CARRA: Copernicus Arctic Regional Reanalysis, https://climate.copernicus.eu/copernicus-arctic-regional-reanalysis-service, 2025.
- 600 Chan, W. C., Shepherd, T. G., Facer-Childs, K., Darch, G., and Arnell, N. W.: Storylines of UK drought based on the 2010-2012 event, Hydrology and Earth System Sciences, 26, https://doi.org/10.5194/hess-26-1755-2022, 2022.
  - Clelland, A. A., Marshall, G. J., and Baxter, R.: Evaluating the performance of key ERA-Interim, ERA5 and ERA5-Land climate variables across Siberia, International Journal of Climatology, 44, 2318–2342, https://doi.org/10.1002/joc.8456, 2024.
  - Computational and Laboratory, I. S.: Cheyenne supercomputer, https://doi.org/10.5065/D6RX99HX, 2019.
- Dai, A., Luo, D., Song, M., and Liu, J.: Arctic amplification is caused by sea-ice loss under increasing CO2, Nature Communications, 10, https://doi.org/10.1038/s41467-018-07954-9, 2019.
  - Danabasoglu, G., Lamarque, J. F., Bacmeister, J., Bailey, D. A., DuVivier, A. K., Edwards, J., Emmons, L. K., Fasullo, J., Garcia, R., Gettelman, A., Hannay, C., Holland, M. M., Large, W. G., Lauritzen, P. H., Lawrence, D. M., Lenaerts, J. T., Lindsay, K., Lipscomb, W. H., Mills, M. J., Neale, R., Oleson, K. W., Otto-Bliesner, B., Phillips, A. S., Sacks, W., Tilmes, S., van Kampenhout, L., Vertenstein,
- M., Bertini, A., Dennis, J., Deser, C., Fischer, C., Fox-Kemper, B., Kay, J. E., Kinnison, D., Kushner, P. J., Larson, V. E., Long, M. C., Mickelson, S., Moore, J. K., Nienhouse, E., Polvani, L., Rasch, P. J., and Strand, W. G.: The Community Earth System Model Version 2 (CESM2), Journal of Advances in Modeling Earth Systems, 12, https://doi.org/10.1029/2019MS001916, 2020.
  - Danielson, J. J. and Gesch, D. B.: Global multi-resolution terrain elevation data 2010 (GMTED2010), Tech. rep., https://doi.org/10.3133/ofr20111073, 2011.
- Datta, R. T., Herrington, A., Lenaerts, J. T., Schneider, D. P., Trusel, L., Yin, Z., and Dunmire, D.: Evaluating the impact of enhanced horizontal resolution over the Antarctic domain using a variable-resolution Earth system model, Cryosphere, 17, https://doi.org/10.5194/tc-17-3847-2023, 2023.
  - Flanner, M. G. and Zender, C. S.: Snowpack radiative heating: Influence on Tibetan Plateau climate, Geophysical Research Letters, 32, L06 501, https://doi.org/10.1029/2004GL022076, 2005.



625

635

640



- Flanner, M. G., Zender, C. S., Randerson, J. T., and Rasch, P. J.: Present-day climate forcing and response from black carbon in snow, Journal of Geophysical Research Atmospheres, 112, https://doi.org/10.1029/2006JD008003, 2007.
  - Gates, W. L., Boyle, J. S., Covey, C., Dease, C. G., Doutriaux, C. M., Drach, R. S., Fiorino, M., Gleckler, P. J., Hnilo, J. J., Marlais, S. M., Phillips, T. J., Potter, G. L., Santer, B. D., Sperber, K. R., Taylor, K. E., and Williams, D. N.: An Overview of the Results of the Atmospheric Model Intercomparison Project (AMIP I), Bulletin of the American Meteorological Society, 80, 29–55, https://doi.org/10.1175/1520-0477(1999)080<0029:AOOTRO>2.0.CO;2, 1999.
  - Gettelman, A. and Morrison, H.: Advanced two-moment bulk microphysics for global models. Part I: Off-line tests and comparison with other schemes, Journal of Climate, 28, https://doi.org/10.1175/JCLI-D-14-00102.1, 2015.
  - Gettelman, A., Morrison, H., Thayer-Calder, K., and Zarzycki, C. M.: The Impact of Rimed Ice Hydrometeors on Global and Regional Climate, Journal of Advances in Modeling Earth Systems, 11, https://doi.org/10.1029/2018MS001488, 2019.
- 630 Guba, O., Taylor, M. A., Ullrich, P. A., Overfelt, J. R., and Levy, M. N.: The spectral element method (SEM) on variable-resolution grids: evaluating grid sensitivity and resolution-aware numerical viscosity, Geoscientific Model Development, 7, 2803–2816, https://doi.org/10.5194/gmd-7-2803-2014, 2014.
  - Guo, Z., Wang, M., Qian, Y., Larson, V. E., Ghan, S., Ovchinnikov, M., Bogenschutz, P. A., Gettelman, A., and Zhou, T.: Parametric behaviors of CLUBB in simulations of low clouds in the Community Atmosphere Model (CAM), Journal of Advances in Modeling Earth Systems, 7, https://doi.org/10.1002/2014MS000405, 2015.
  - Hawkins, E. and Sutton, R.: The potential to narrow uncertainty in regional climate predictions, Bulletin of the American Meteorological Society, 90, https://doi.org/10.1175/2009BAMS2607.1, 2009.
  - Herrington, A. R., Lauritzen, P. H., Lofverstrom, M., Lipscomb, W. H., Gettelman, A., and Taylor, M. A.: Impact of Grids and Dynamical Cores in CESM2.2 on the Surface Mass Balance of the Greenland Ice Sheet, Journal of Advances in Modeling Earth Systems, 14, https://doi.org/10.1029/2022MS003192, 2022.
  - Hersbach, H., Bell, B., Berrisford, P., Hirahara, S., Horányi, A., Muñoz-Sabater, J., Nicolas, J., Peubey, C., Radu, R., Schepers, D., Simmons, A., Soci, C., Abdalla, S., Abellan, X., Balsamo, G., Bechtold, P., Biavati, G., Bidlot, J., Bonavita, M., De Chiara, G., Dahlgren, P., Dee, D., Diamantakis, M., Dragani, R., Flemming, J., Forbes, R., Fuentes, M., Geer, A., Haimberger, L., Healy, S., Hogan, R. J., Hólm, E., Janisková, M., Keeley, S., Laloyaux, P., Lopez, P., Lupu, C., Radnoti, G., de Rosnay, P., Rozum, I., Vamborg, F., Villaume, S., and Thépaut, J.-N.: The ERA5 global reanalysis, Quarterly Journal of the Royal Meteorological Society, 146, 1999–2049, https://doi.org/10.1002/qj.3803, 2020.
  - Hirabayashi, Y., Mahendran, R., Koirala, S., Konoshima, L., Yamazaki, D., Watanabe, S., Kim, H., and Kanae, S.: Global flood risk under climate change, Nature Climate Change, 3, 816–821, https://doi.org/10.1038/nclimate1911, nULL, 2013.
- Huang, X., Gettelman, A., Skamarock, W. C., Lauritzen, P. H., Curry, M., Herrington, A., Truesdale, J. T., and Duda, M.: Advancing precipitation prediction using a new-generation storm-resolving model framework SIMA-MPAS (V1.0): a case study over the western United States, Geoscientific Model Development, 15, https://doi.org/10.5194/gmd-15-8135-2022, 2022.
  - Hurtt, G. C., Chini, L., Sahajpal, R., Frolking, S., Bodirsky, B. L., Calvin, K., Doelman, J. C., Fisk, J., Fujimori, S., Goldewijk, K. K., Hasegawa, T., Havlik, P., Heinimann, A., Humpenöder, F., Jungclaus, J., Kaplan, J. O., Kennedy, J., Krisztin, T., Lawrence, P., Ma, L., Mertz, O., Pongratz, J., Popp, A., Poulter, B., Riahi, K., Shevliakova, E., Stehfest, E., Thornton, P., Tubiello, F. N., van Vuuren,
- D. P., and Zhang, X.: Harmonization of global land use change and management for the period 850-2100 (LUH2) for CMIP6, Geoscientific Model Development, 13, https://doi.org/10.5194/gmd-13-5425-2020, 2020.





- Iacono, M. J., Delamere, J. S., Mlawer, E. J., Shephard, M. W., Clough, S. A., and Collins, W. D.: Radiative forcing by long-lived greenhouse gases: Calculations with the AER radiative transfer models, Journal of Geophysical Research Atmospheres, 113, https://doi.org/10.1029/2008JD009944, 2008.
- Johnson, N. C., Xie, S. P., Kosaka, Y., and Li, X.: Increasing occurrence of cold and warm extremes during the recent global warming slowdown, Nature Communications, 9, https://doi.org/10.1038/s41467-018-04040-y, 2018.
  - Kim, B. M., Son, S. W., Min, S. K., Jeong, J. H., Kim, S. J., Zhang, X., Shim, T., and Yoon, J. H.: Weakening of the stratospheric polar vortex by Arctic sea-ice loss, Nature Communications, 5, https://doi.org/10.1038/ncomms5646, 2014.
- Kim, Y. H., Min, S. K., Zhang, X., Sillmann, J., and Sandstad, M.: Evaluation of the CMIP6 multi-model ensemble for climate extreme indices, Weather and Climate Extremes, 29, https://doi.org/10.1016/j.wace.2020.100269, 2020.
  - Klein-Goldewijk, K., Beusen, A., Doelman, J., and Stehfest, E.: Anthropogenic land use estimates for the Holocene HYDE 3.2, Earth System Science Data, 9, https://doi.org/10.5194/essd-9-927-2017, 2017.
  - Kosaka, Y., Kobayashi, S., Harada, Y., Kobayashi, C., Naoe, H., Yoshimoto, K., Harada, M., Goto, N., Chiba, J., Miyaoka, K., Sekiguchi, R., Deushi, M., Kamahori, H., Nakaegawa, T., Tanaka, T. Y., Tokuhiro, T., Sato, Y., Matsushita, Y., and Onogi, K.: The JRA-3Q reanalysis, Journal of the Meteorological Society of Japan, 102, https://doi.org/10.2151/jmsj.2024-004, 2024.
  - Kug, J. S., Jeong, J. H., Jang, Y. S., Kim, B. M., Folland, C. K., Min, S. K., and Son, S. W.: Two distinct influences of Arctic warming on cold winters over North America and East Asia, Nature Geoscience, 8, https://doi.org/10.1038/ngeo2517, 2015.
  - Köhler, D., Räisänen, P., Naakka, T., Nordling, K., and Sinclair, V. A.: The future North Atlantic jet stream and storm track: relative contributions from sea ice and sea surface temperature changes, EGUSphere, https://doi.org/10.5194/egusphere-2024-3713, 2024.
- Landrum, L. and Holland, M. M.: Extremes become routine in an emerging new Arctic, Nature Climate Change, 10, https://doi.org/10.1038/s41558-020-0892-z, 2020.
  - Lauritzen, P. H., Bacmeister, J. T., Callaghan, P. F., and Taylor, M. A.: NCAR\_Topo (v1.0): NCAR global model topography generation software for unstructured grids, https://doi.org/10.5194/gmd-8-3975-2015, 2015.
- Lauritzen, P. H., Nair, R. D., Herrington, A. R., Callaghan, P., Goldhaber, S., Dennis, J. M., Bacmeister, J. T., Eaton, B. E., Zarzycki, C. M.,
   Taylor, M. A., Ullrich, P. A., Dubos, T., Gettelman, A., Neale, R. B., Dobbins, B., Reed, K. A., Hannay, C., Medeiros, B., Benedict, J. J., and Tribbia, J. J.: NCAR Release of CAM-SE in CESM2.0: A Reformulation of the Spectral Element Dynamical Core in Dry-Mass Vertical Coordinates With Comprehensive Treatment of Condensates and Energy, Journal of Advances in Modeling Earth Systems, 10, https://doi.org/10.1029/2017MS001257, 2018.
- Lawrence, D. M., Fisher, R. A., Koven, C. D., Oleson, K. W., Swenson, S. C., Bonan, G., Collier, N., Ghimire, B., Kampenhout, L.,
  Kennedy, D., Kluzek, E., Lawrence, P. J., Li, F., Li, H., Lombardozzi, D., Riley, W. J., Sacks, W. J., Shi, M., Vertenstein, M., Wieder, W. R., Xu, C., Ali, A. A., Badger, A. M., Bisht, G., Broeke, M., Brunke, M. A., Burns, S. P., Buzan, J., Clark, M., Craig, A., Dahlin, K., Drewniak, B., Fisher, J. B., Flanner, M., Fox, A. M., Gentine, P., Hoffman, F., Keppel-Aleks, G., Knox, R., Kumar, S., Lenaerts, J., Leung, L. R., Lipscomb, W. H., Lu, Y., Pandey, A., Pelletier, J. D., Perket, J., Randerson, J. T., Ricciuto, D. M., Sanderson, B. M., Slater, A., Subin, Z. M., Tang, J., Thomas, R. Q., Martin, M. V., and Zeng, X.: The Community Land Model Version 5: Description of New Features, Benchmarking, and Impact of Forcing Uncertainty, Journal of Advances in Modeling Earth Systems, 11, 4245–4287, https://doi.org/10.1029/2018MS001583, 2019.
  - Lee, J.-Y., Marotzke, J., Bala, G., Cao, L., Corti, S., Dunne, J., Engelbrecht, F., Fischer, E., Fyfe, J., Jones, C., Maycock, A., Mutemi, J., Ndiaye, O., Panickal, S., and Zhou, T.: Future Global Climate: Scenario-based Projections and Near-term Information, pp. 553–672, Cambridge University Press, https://doi.org/10.1017/9781009157896.006, 2021.



705

720



- Levine, X. J., Williams, R. S., Marshall, G., Orr, A., Graff, L. S., Handorf, D., Karpechko, A., Köhler, R., Wijngaard, R. R., Johnston, N., Lee, H., Nieradzik, L., and Mooney, P. A.: Storylines of summer Arctic climate change constrained by Barents-Kara seas and Arctic tropospheric warming for climate risk assessment, Earth System Dynamics, 15, 1161–1177, https://doi.org/10.5194/esd-15-1161-2024, 2024.
- Lin, Y., Dong, W., Zhang, M., Xie, Y., Xue, W., Huang, J., and Luo, Y.: Causes of model dry and warm bias over central U.S. and impact on climate projections, Nature Communications, 8, 881, https://doi.org/10.1038/s41467-017-01040-2, 2017.
  - Liu, W., Fedorov, A. V., Xie, S. P., and Hu, S.: Climate impacts of a weakened Atlantic meridional overturning circulation in a warming climate, Science Advances, 6, https://doi.org/10.1126/sciadv.aaz4876, 2020.
  - Liu, X., Ma, P. L., Wang, H., Tilmes, S., Singh, B., Easter, R. C., Ghan, S. J., and Rasch, P. J.: Description and evaluation of a new four-mode version of the Modal Aerosol Module (MAM4) within version 5.3 of the Community Atmosphere Model, Geoscientific Model Development, 9, https://doi.org/10.5194/gmd-9-505-2016, 2016.
  - Loeb, N. A., Crawford, A., Herrington, A., McCrystall, M., Stroeve, J., and Hanesiak, J.: Projections and Physical Drivers of Extreme Precipitation in Greenland Baffin Bay, Journal of Geophysical Research: Atmospheres, 129, https://doi.org/10.1029/2024JD041375, 2024.
- Lorenz, R., Argüeso, D., Donat, M. G., Pitman, A. J., Hurk, B. V. D., Berg, A., Lawrence, D. M., Chéruy, F., Ducharne, A., Hagemann, S.,
  Meier, A., Milly, P. C., and Seneviratne, S. I.: Influence of land-atmosphere feedbacks on temperature and precipitation extremes in the
  GLACE-CMIP5 ensemble, Journal of Geophysical Research, 121, https://doi.org/10.1002/2015JD024053, 2016.
  - Masrur, A., Petrov, A. N., and DeGroote, J.: Circumpolar spatio-temporal patterns and contributing climatic factors of wildfire activity in the Arctic tundra from 2001-2015, https://doi.org/10.1088/1748-9326/aa9a76, 2018.
- Matthes, H., Rinke, A., and Dethloff, K.: Recent changes in Arctic temperature extremes: Warm and cold spells during winter and summer,

  Environmental Research Letters, 10, https://doi.org/10.1088/1748-9326/10/11/114020, 2015.
  - McCrystall, M. R., Stroeve, J., Serreze, M., Forbes, B. C., and Screen, J. A.: New climate models reveal faster and larger increases in Arctic precipitation than previously projected, Nature Communications, 12, https://doi.org/10.1038/s41467-021-27031-y, 2021.
  - Mindlin, J., Shepherd, T. G., Vera, C. S., Osman, M., Zappa, G., Lee, R. W., and Hodges, K. I.: Storyline description of Southern Hemisphere midlatitude circulation and precipitation response to greenhouse gas forcing, Climate Dynamics, 54, https://doi.org/10.1007/s00382-020-05234-1, 2020.
  - Morlighem, M., Williams, C. N., Rignot, E., An, L., Arndt, J. E., Bamber, J. L., Catania, G., Chauché, N., Dowdeswell, J. A., Dorschel, B., Fenty, I., Hogan, K., Howat, I., Hubbard, A., Jakobsson, M., Jordan, T. M., Kjeldsen, K. K., Millan, R., Mayer, L., Mouginot, J., Noël, B. P., O'Cofaigh, C., Palmer, S., Rysgaard, S., Seroussi, H., Siegert, M. J., Slabon, P., Straneo, F., van den Broeke, M. R., Weinrebe, W., Wood, M., and Zinglersen, K. B.: BedMachine v3: Complete Bed Topography and Ocean Bathymetry Mapping of Greenland From Multibeam Echo Sounding Combined With Mass Conservation, Geophysical Research Letters, 44, https://doi.org/10.1002/2017GL074954, 2017.
- Morlighem, M., Rignot, E., Binder, T., Blankenship, D., Drews, R., Eagles, G., Eisen, O., Ferraccioli, F., Forsberg, R., Fretwell, P., Goel, V., Greenbaum, J. S., Gudmundsson, H., Guo, J., Helm, V., Hofstede, C., Howat, I., Humbert, A., Jokat, W., Karlsson, N. B., Lee, W. S., Matsuoka, K., Millan, R., Mouginot, J., Paden, J., Pattyn, F., Roberts, J., Rosier, S., Ruppel, A., Seroussi, H., Smith, E. C., Steinhage, D., Sun, B., den Broeke, M. R., Ommen, T. D., van Wessem, M., and Young, D. A.: Deep glacial troughs and stabilizing ridges unveiled beneath the margins of the Antarctic ice sheet, Nature Geoscience, 13, https://doi.org/10.1038/s41561-019-0510-8, 2020.





- O'Brien, T. A., Collins, W. D., Kashinath, K., Rübel, O., Byna, S., Gu, J., Krishnan, H., and Ullrich, P. A.: Resolution dependence of precipitation statistical fidelity in hindcast simulations, Journal of Advances in Modeling Earth Systems, 8, https://doi.org/10.1002/2016MS000671, 2016.
- Oleson, K., Lawrence, D., Bonan, G., Drewniak, B., Huang, M., C.D., K., Levis, S., Li, F., Riley, W., Subin, Z., Swenson, S., P.E., T.,

  Bozbiyik, A., Fisher, R., Heald, C., Kluzek, E., Lamarque, J.-F., Leung, L. R., Lipscomb, W., Muszala, S., Ricciuto, D., Sacks, W., Tang,
  J., and Yang, Z.-L.: Technical description of version 4.5 of the Community Land Model (CLM). Ncar Tech. Note NCAR/TN-503+STR.

  National Center for Atmospheric Research, Boulder, Geophysical Research Letters, 37, 1–434, https://doi.org/10.5065/D6RR1W7M,
  2013.
- Overland, J., Dunlea, E., Box, J. E., Corell, R., Forsius, M., Kattsov, V., Olsen, M. S., Pawlak, J., Reiersen, L. O., and Wang, M.: The urgency of Arctic change, https://doi.org/10.1016/j.polar.2018.11.008, 2019.
  - Overland, J. E.: Arctic Climate Extremes, https://doi.org/10.3390/atmos13101670, 2022.
  - Paik, S., An, S. I., Min, S. K., King, A. D., and Kim, S. K.: Emergent constraints on future extreme precipitation intensification: from global to continental scales, Weather and Climate Extremes, 42, https://doi.org/10.1016/j.wace.2023.100613, 2023.
- Park, H. S., Kim, S. J., Stewart, A. L., Son, S. W., and Seo, K. H.: Mid-Holocene Northern Hemisphere warming driven by Arctic amplification, Science Advances, 5, https://doi.org/10.1126/sciadv.aax8203, 2019.
  - Pfahl, S., O'Gorman, P. A., and Fischer, E. M.: Understanding the regional pattern of projected future changes in extreme precipitation, Nature Climate Change, 7, https://doi.org/10.1038/nclimate3287, 2017.
  - Previdi, M., Smith, K. L., and Polvani, L. M.: Arctic amplification of climate change: A review of underlying mechanisms, https://doi.org/10.1088/1748-9326/ac1c29, 2021.
- Rantanen, M., Karpechko, A. Y., Lipponen, A., Nordling, K., Hyvärinen, O., Ruosteenoja, K., Vihma, T., and Laaksonen, A.: The Arctic has warmed nearly four times faster than the globe since 1979, Communications Earth and Environment, 3, https://doi.org/10.1038/s43247-022-00498-3, 2022.
  - Rhoades, A. M., Huang, X., Ullrich, P. A., and Zarzycki, C. M.: Characterizing Sierra Nevada Snowpack Using Variable-Resolution CESM, Journal of Applied Meteorology and Climatology, 55, 173–196, https://doi.org/10.1175/JAMC-D-15-0156.1, 2016.
- Rhoades, A. M., Ullrich, P. A., Zarzycki, C. M., Johansen, H., Margulis, S. A., Morrison, H., Xu, Z., and Collins, W. D.: Sensitivity of Mountain Hydroclimate Simulations in Variable-Resolution CESM to Microphysics and Horizontal Resolution, Journal of Advances in Modeling Earth Systems, 10, 1357–1380, https://doi.org/10.1029/2018MS001326, 2018.
  - Screen, J. A. and Simmonds, I.: The central role of diminishing sea ice in recent Arctic temperature amplification, Nature, 464, https://doi.org/10.1038/nature09051, 2010.
- Screen, J. A., Deser, C., and Sun, L.: Projected changes in regional climate extremes arising from Arctic sea ice loss, Environmental Research Letters, 10, https://doi.org/10.1088/1748-9326/10/8/084006, 2015.
  - Séférian, R., Nabat, P., Michou, M., Saint-Martin, D., Voldoire, A., Colin, J., Decharme, B., Delire, C., Berthet, S., Chevallier, M., Sénési, S., Franchisteguy, L., Vial, J., Mallet, M., Joetzjer, E., Geoffroy, O., Guérémy, J.-F., Moine, M.-P., Msadek, R., Ribes, A., Rocher, M., Roehrig, R., Salas-y Mélia, D., Sanchez, E., Terray, L., Valcke, S., Waldman, R., Aumont, O., Bopp, L., Deshayes, J., Éthé, C., and
- Madec, G.: Evaluation of CNRM Earth System Model, CNRM-ESM2-1: Role of Earth System Processes in Present-Day and Future Climate, Journal of Advances in Modeling Earth Systems, 11, 4182–4227, https://doi.org/10.1029/2019MS001791, 2019.
  - Seland, Ø., Bentsen, M., Olivié, D., Toniazzo, T., Gjermundsen, A., Graff, L. S., Debernard, J. B., Gupta, A. K., He, Y.-C., Kirkevåg, A., Schwinger, J., Tjiputra, J., Aas, K. S., Bethke, I., Fan, Y., Griesfeller, J., Grini, A., Guo, C., Ilicak, M., Karset, I. H. H., Landgren,



780



- O., Liakka, J., Moseid, K. O., Nummelin, A., Spensberger, C., Tang, H., Zhang, Z., Heinze, C., Iversen, T., and Schulz, M.: Overview of the Norwegian Earth System Model (NorESM2) and key climate response of CMIP6 DECK, historical, and scenario simulations, Geoscientific Model Development, 13, 6165–6200, https://doi.org/10.5194/gmd-13-6165-2020, 2020.
  - Seneviratne, S., Nicholls, N., Easterling, D., Goodess, C., Kanae, S., Kossin, J., Luo, Y., Marengo, J., McInnes, K., Rahimi, M., Reichstein, M., Sorteberg, A., Vera, C., and Zhang, X.: Changes in Climate Extremes and their Impacts on the Natural Physical Environment, pp. 109–230, Cambridge University Press, ISBN 1107025060, https://doi.org/10.1017/CBO9781139177245.006, nULL, 2012.
- Seneviratne, S. I. and Hauser, M.: Regional Climate Sensitivity of Climate Extremes in CMIP6 Versus CMIP5 Multimodel Ensembles, Earth's Future, 8, https://doi.org/10.1029/2019EF001474, 2020.
  - Seneviratne, S. I., Zhang, X., Adnan, M., Badi, W., Dereczynski, C., Luca, A. D., Ghosh, S., Iskandar, I., Kossin, J., Lewis, S., Otto, F., Pinto, I., Satoh, M., Vicente-Serrano, S. M., Wehner, M., and Zhou, B.: Weather and Climate Extreme Events in a Changing Climate, pp. 1513–1766, Cambridge University Press, Cambridge, United Kingdom and New York, NY, USA, https://doi.org/10.1017/9781009157896.013, 2021.
  - Shaw, J., McGraw, Z., Bruno, O., Storelvmo, T., and Hofer, S.: Using Satellite Observations to Evaluate Model Microphysical Representation of Arctic Mixed-Phase Clouds, Geophysical Research Letters, 49, e2021GL096191, https://doi.org/10.1029/2021GL096191, e2021GL096191 2021GL096191, 2022.
- Shepherd, T. G., Boyd, E., Calel, R. A., Chapman, S. C., Dessai, S., Dima-West, I. M., Fowler, H. J., James, R., Maraun, D., Martius,
  O., Senior, C. A., Sobel, A. H., Stainforth, D. A., Tett, S. F., Trenberth, K. E., van den Hurk, B. J., Watkins, N. W., Wilby, R. L., and Zenghelis, D. A.: Storylines: an alternative approach to representing uncertainty in physical aspects of climate change, Climatic Change, 151, https://doi.org/10.1007/s10584-018-2317-9, 2018.
  - Sillmann, J., Kharin, V., Zhang, X., Zwiers, F., and Bronaugh, D.: Climate extremes indices in the CMIP5 multimodel ensemble: Part 1. Model evaluation in the present climate, Journal of Geophysical Research Atmospheres, 118, 1716–1733, https://doi.org/10.1002/jgrd.50203, 2013a.
  - Sillmann, J., Kharin, V., Zwiers, F., Zhang, X., and Bronaugh, D.: Climate extremes indices in the CMIP5 multimodel ensemble: Part 2. Future climate projections, Journal of Geophysical Research Atmospheres, 118, 2473–2493, https://doi.org/10.1002/jgrd.50188, 2013b.
  - Sillmann, J., Shepherd, T. G., van den Hurk, B., Hazeleger, W., Martius, O., Slingo, J., and Zscheischler, J.: Event-Based Storylines to Address Climate Risk, https://doi.org/10.1029/2020EF001783, 2021.
- Skamarock, W. C., Snyder, C., Klemp, J. B., and Park, S. H.: Vertical resolution requirements in atmospheric simulation, Monthly Weather Review, 147, https://doi.org/10.1175/MWR-D-19-0043.1, 2019.
  - Smirnov, D., Newman, M., Alexander, M. A., Kwon, Y.-O., and Frankignoul, C.: Investigating the Local Atmospheric Response to a Realistic Shift in the Oyashio Sea Surface Temperature Front, Journal of Climate, 28, 1126–1147, https://doi.org/10.1175/JCLI-D-14-00285.1, 2015.
- 800 Ullrich, P.: SQuadGen: spherical quadrilateral grid generator, https://climate.ucdavis.edu/squadgen.php, 2014.
  - van Dalum, C. T., van de Berg, W. J., Gadde, S. N., van Tiggelen, M., van der Drift, T., van Meijgaard, E., van Ulft, L. H., and van den Broeke, M. R.: First results of the polar regional climate model RACMO2.4, The Cryosphere, 18, 4065–4088, https://doi.org/10.5194/tc-18-4065-2024, 2024.
- van Kampenhout, L., Lenaerts, J. T. M., Lipscomb, W. H., Sacks, W. J., Lawrence, D. M., Slater, A. G., and van den Broeke, M. R.: Improving the Representation of Polar Snow and Firn in the Community Earth System Model, Journal of Advances in Modeling Earth Systems, 9, 2583–2600, https://doi.org/10.1002/2017MS000988, 2017.





- van Kampenhout, L., Rhoades, A. M., Herrington, A. R., Zarzycki, C. M., Lenaerts, J. T. M., Sacks, W. J., and van den Broeke, M. R.: Regional grid refinement in an Earth system model: impacts on the simulated Greenland surface mass balance, The Cryosphere, 13, 1547–1564, https://doi.org/10.5194/tc-13-1547-2019, 2019.
- Waling, A., Herrington, A., Duderstadt, K., Dibb, J., and Burakowski, E.: Using variable-resolution grids to model precipitation from atmospheric rivers around the Greenland ice sheet, Weather and Climate Dynamics, 5, 1117–1135, https://doi.org/10.5194/wcd-5-1117-2024, 2024.
  - Walsh, J. E., Ballinger, T. J., Euskirchen, E. S., Hanna, E., Mård, J., Overland, J. E., Tangen, H., and Vihma, T.: Extreme weather and climate events in northern areas: A review, Earth-Science Reviews, 209, https://doi.org/10.1016/j.earscirev.2020.103324, 2020.
- Wehner, M. F., Reed, K. A., Li, F., Prabhat, Bacmeister, J., Chen, C. T., Paciorek, C., Gleckler, P. J., Sperber, K. R., Collins, W. D., Gettelman, A., and Jablonowski, C.: The effect of horizontal resolution on simulation quality in the Community Atmospheric Model, CAM5.1, Journal of Advances in Modeling Earth Systems, 6, https://doi.org/10.1002/2013MS000276, 2014.
  - Weijer, W., Cheng, W., Garuba, O. A., Hu, A., and Nadiga, B. T.: CMIP6 Models Predict Significant 21st Century Decline of the Atlantic Meridional Overturning Circulation, Geophysical Research Letters, 47, https://doi.org/10.1029/2019GL086075, 2020.
- Weimer, M., Wilka, C., Kinnison, D. E., Garcia, R. R., Bacmeister, J. T., Alexander, M. J., Dörnbrack, A., and Solomon, S.: A Method for Estimating Global Subgrid-Scale Orographic Gravity-Wave Temperature Perturbations in Chemistry-Climate Models, Journal of Advances in Modeling Earth Systems, 15, https://doi.org/10.1029/2022MS003505, 2023.
  - Wijngaard, R. R., Herrington, A. R., Lipscomb, W. H., Leguy, G. R., and An, S. I.: Exploring the ability of the variable-resolution Community Earth System Model to simulate cryospheric-hydrological variables in High Mountain Asia, Cryosphere, 17, https://doi.org/10.5194/tc-17-3803-2023, 2023.
  - Williams, R. S., Marshall, G. J., Levine, X., Graff, L. S., Handorf, D., Johnston, N. M., Karpechko, A. Y., Andrew, O. R., van de Berg, W. J., Wijngaard, R. R., and Mooney, P. A.: Future Antarctic Climate: Storylines of Midlatitude Jet Strengthening and Shift Emergent from CMIP6, Journal of Climate, 37, https://doi.org/10.1175/JCLI-D-23-0122.1, 2024.
- Wills, R. C. J., Herrington, A. R., Simpson, I. R., and Battisti, D. S.: Resolving Weather Fronts Increases the Large-Scale Circulation Response to Gulf Stream SST Anomalies in Variable-Resolution CESM2 Simulations, Journal of Advances in Modeling Earth Systems, 16, https://doi.org/10.1029/2023MS004123, 2024.
  - Xu, Z., Chang, A., and Vittorio, A. D.: Evaluating and projecting of climate extremes using a variable-resolution global climate model (VR-CESM), Weather and Climate Extremes, 38, https://doi.org/10.1016/j.wace.2022.100496, 2022.
- Yin, Z., Herrington, A. R., Datta, R., Subramanian, A. C., Lenaerts, J. T. M., and Gettelman, A.: Improved Understanding of Multicentury

  Greenland Ice Sheet Response to Strong Warming in the Coupled CESM2-CISM2 with Regional Grid Refinement, Journal of Advances in Modeling Earth Systems, https://doi.org/10.22541/au.170967825.56554188/v1, 2024.
  - Zampieri, L., Arduini, G., Holland, M., Keeley, S. P., Mogensen, K., Shupe, M. D., and Tietsche, S.: A Machine Learning Correction Model of the Winter Clear-Sky Temperature Bias over the Arctic Sea Ice in Atmospheric Reanalyses, Monthly Weather Review, 151, https://doi.org/10.1175/MWR-D-22-0130.1, 2023.
- Zappa, G.: Regional Climate Impacts of Future Changes in the Mid–Latitude Atmospheric Circulation: a Storyline View, Current Climate Change Reports, 5, https://doi.org/10.1007/s40641-019-00146-7, 2019.
  - Zappa, G. and Shepherd, T. G.: Storylines of atmospheric circulation change for European regional climate impact assessment, Journal of Climate, 30, https://doi.org/10.1175/JCLI-D-16-0807.1, 2017.





- Zarzycki, C. M. and Jablonowski, C.: A multidecadal simulation of Atlantic tropical cyclones using a variable-resolution global atmospheric general circulation model, Journal of Advances in Modeling Earth Systems, 6, 805–828, https://doi.org/10.1002/2014MS000352, 2014.
  - Zarzycki, C. M., Levy, M. N., Jablonowski, C., Overfelt, J. R., Taylor, M. A., and Ullrich, P. A.: Aquaplanet Experiments Using CAM's Variable-Resolution Dynamical Core, Journal of Climate, 27, 5481–5503, https://doi.org/10.1175/JCLI-D-14-00004.1, 2014.
  - Zhang, G. J. and McFarlane, N. A.: Sensitivity of climate simulations to the parameterization of cumulus convection in the canadian climate centre general circulation model, Atmosphere Ocean, 33, https://doi.org/10.1080/07055900.1995.9649539, 1995.
- Zhu, H., Zhang, J., Xu, Z., Vittorio, A. V. D., Xin, X., Xiao, C., and Li, Y.: Advantages of a variable-resolution global climate model in reproducing the seasonal evolution of East Asian summer monsoon, International Journal of Climatology, 43, https://doi.org/10.1002/joc.7796, 2023.
- Zhu, J., Otto-Bliesner, B. L., Brady, E. C., Gettelman, A., Bacmeister, J. T., Neale, R. B., Poulsen, C. J., Shaw, J. K., McGraw, Z. S., and Kay, J. E.: LGM Paleoclimate Constraints Inform Cloud Parameterizations and Equilibrium Climate Sensitivity in CESM2, Journal of Advances in Modeling Earth Systems, 14, https://doi.org/10.1029/2021MS002776, 2022.





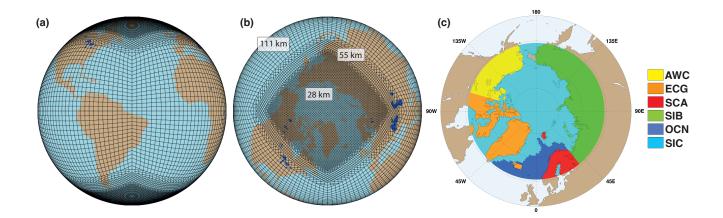


**Figure 1.** Schematic representation of the variable resolution (VR) spectral element grid (**a**) with regional grid refinements over the Arctic (**b**), and an overview of regions used for analysis throughout this study (**c**), which include four land regions AWC (Alaska and Western Canada; yellow), ECG (Eastern Canada and Greenland; orange), SCA (Scandinavia; red), and SIB (Siberia; green), a sea ice region (SIC; diagonal pattern), and an ocean region (OCN; crossed pattern).





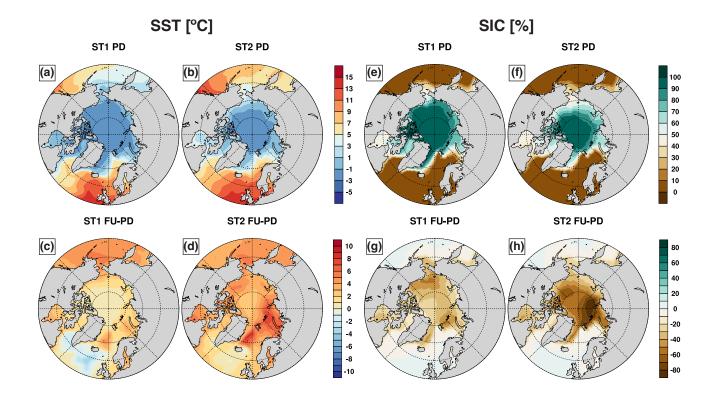


**Figure 2.** Present-day B (2005–2014) state (**a-b,e-f**) and future (2090–2099) changes (**c-d,g-h**) in northern hemisphere (poleward of 50°N) sea surface temperature (SST (°C); **a-d**) and sea ice cover (SIC (%); **e-h**) as outputted by the NE30 grid for two different storylines: ST1 (**a,c,e,g**) and ST2 (**b,d,f,h**). The future changes are expressed as absolute differences relative to present-day.





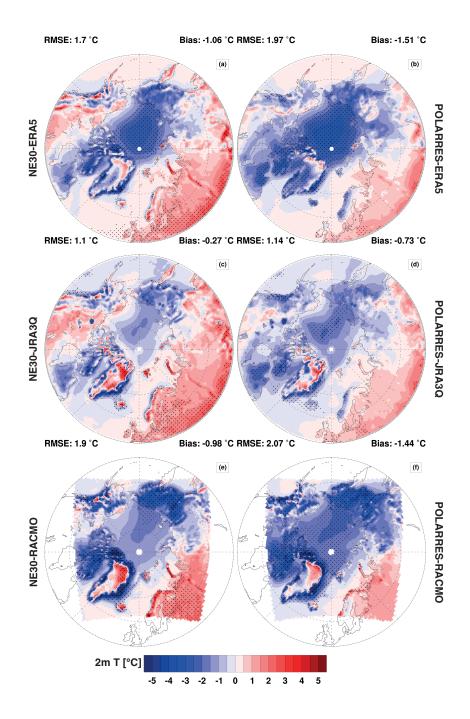


**Figure 3.** Present-day A (1985–2014) northern hemisphere (poleward of 50°N) annual mean 2m temperature (°C) differences between NE30 and ERA5 (**a**), JRA-3Q (**c**) or RACMO (**e**), and between POLARRES and ERA5 (**b**), JRA-3Q (**d**), or RACMO (**f**). The area-weighted root-mean-square-error (RMSE) and mean bias listed above the panels are calculated for the domain 60-90°N. The dots represent the significance of temperature differences at the 95% confidence level.





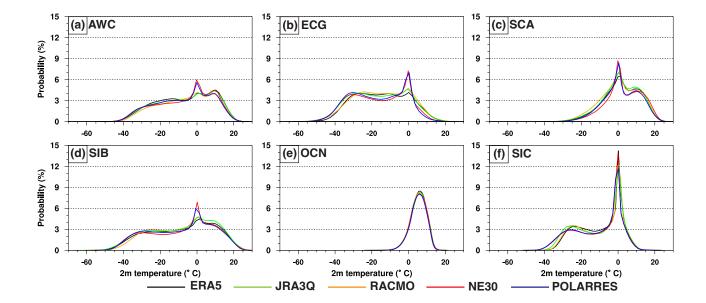


**Figure 4.** Present-day A (1985–2014) annual 2m temperature (°C) probability density functions (PDFs) for NE30 (red), POLARRES (blue), ERA5 (black), JRA-3Q (green), and RACMO (orange). The PDFs are calculated on a NE30 grid for the six different regions as shown in Fig. 1.





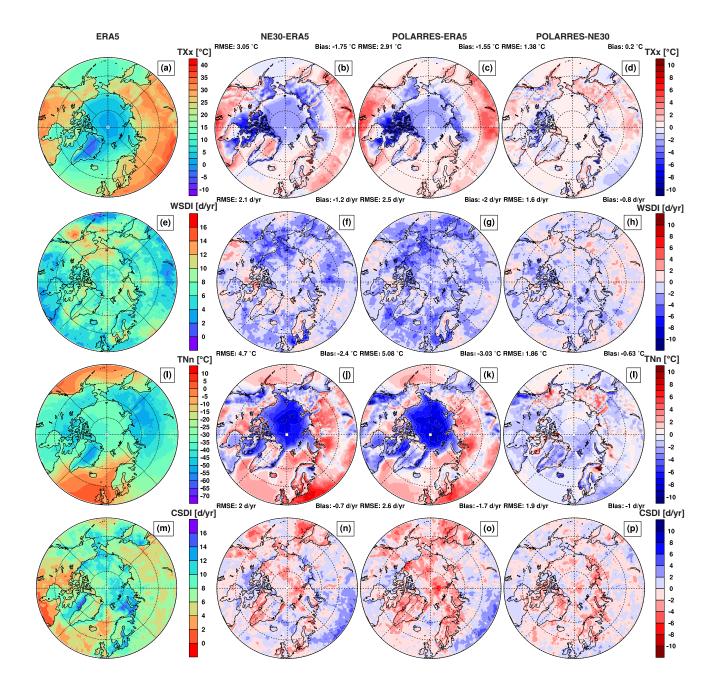
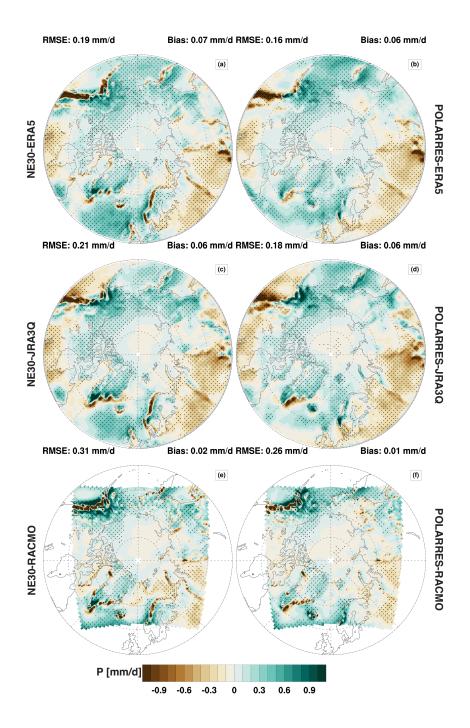


Figure 5. Present-day A (1985–2014) northern hemisphere (poleward of  $50^{\circ}$ N) annual maximum of TX (TXx (°C); **a-d**), warm spell duration index (WSDI ( $dyr^{-1}$ ); **e-h**), annual minimum of TN (TNn (°C); **j-l**), and cold spell duration index (CSDI ( $dyr^{-1}$ ); **m-p**) state ( $1^{st}$  column) and differences between NE30 and ERA5 ( $2^{nd}$  column), POLARRES and ERA5 ( $3^{rd}$  column), and POLARRES and NE30 ( $4^{th}$  column). The area-weighted root-mean-square-difference (RMSE) and mean bias listed above the  $2^{nd}$ - $4^{th}$  column panels are calculated for the domain 60- $90^{\circ}$ N.







**Figure 6.** Same as Fig. 3, but for annual mean precipitation  $(mm d^{-1})$ 





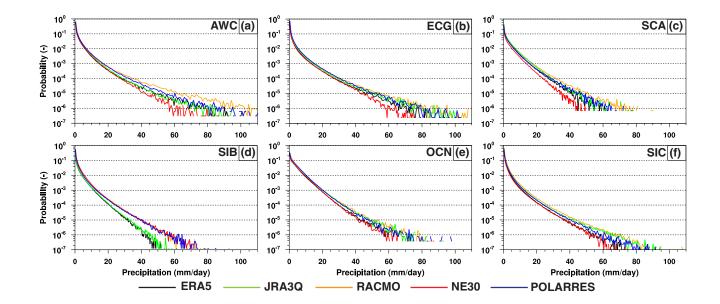


**Figure 7.** Same as Fig. 4, but for daily precipitation rates  $(mm d^{-1})$ 





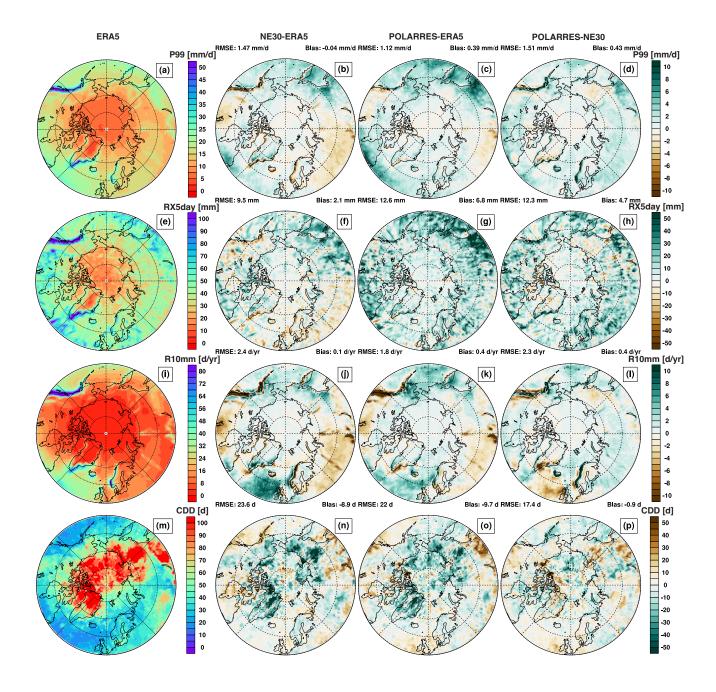


**Figure 8.** Same as Fig.5, but for the  $99^{th}$  percentile of daily precipitation (P99 (mm d<sup>-1</sup>); **a-d**), highest 5-day precipitation (RX5day (mm); **e-h**), heavy precipitation days (R10mm (d yr<sup>-1</sup>); **i-l**), and consecutive dry days (CDD (d); **m-p**)





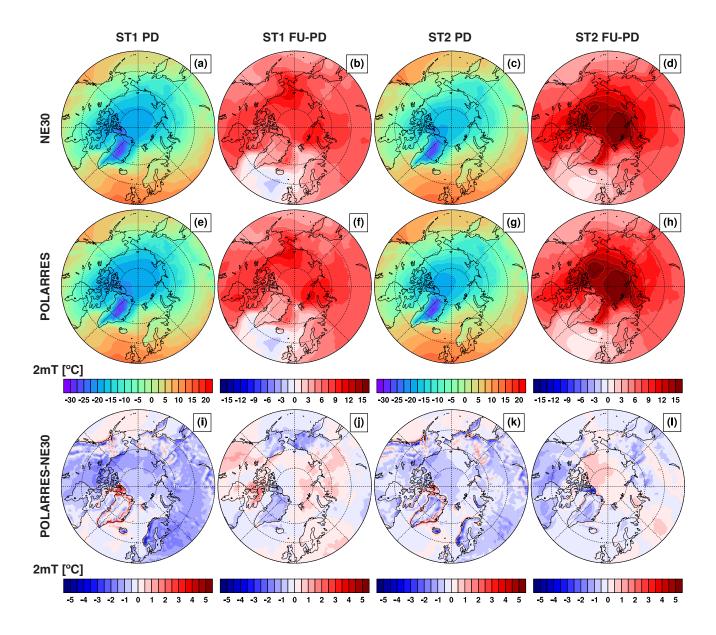


**Figure 9.** Northern hemisphere (poleward of  $50^{\circ}$ N) present-day B (2005-2014) annual 2m temperature and projected future (2090-2099) changes in annual 2m temperature ( $^{\circ}$ C) for NE30 (**a-d**) and POLARRES (**e-h**) in ST1 ( $1^{st}$  and  $2^{nd}$  columns) and ST2 ( $3^{rd}$  and  $4^{th}$  columns). The future changes are expressed as absolute differences relative to present-day. The differences between NE30 and POLARRES are shown in the bottom row (**i-l**).





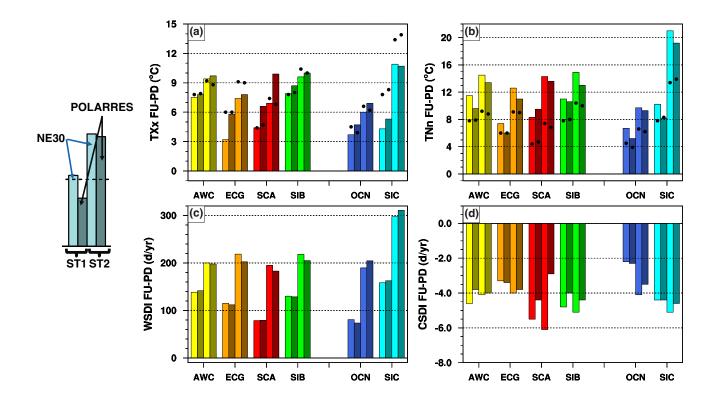


**Figure 10.** Projected future (2090–2099) changes in annual maximum temperature (TXx ( $^{\circ}$ C); **a**), annual minimum temperature (TNn ( $^{\circ}$ C; **b**), warm spell duration index (WSDI ( $^{\circ}$ dyr<sup>-1</sup>); **c**), and cold spell duration index (CSDI ( $^{\circ}$ dyr<sup>-1</sup>); **d**) for six different regions as shown in Fig. 1. The bars show the projected changes in NE30 ( $^{st}$  and  $^{st}$  bars) and POLARRES ( $^{st}$  and  $^{st}$  bars) for ST1 ( $^{st}$  and  $^{st}$  bars) and ST2 ( $^{st}$  and  $^{st}$  bars). The black dots denote the projected changes in annual mean near-surface temperature ( $^{\circ}$ C).





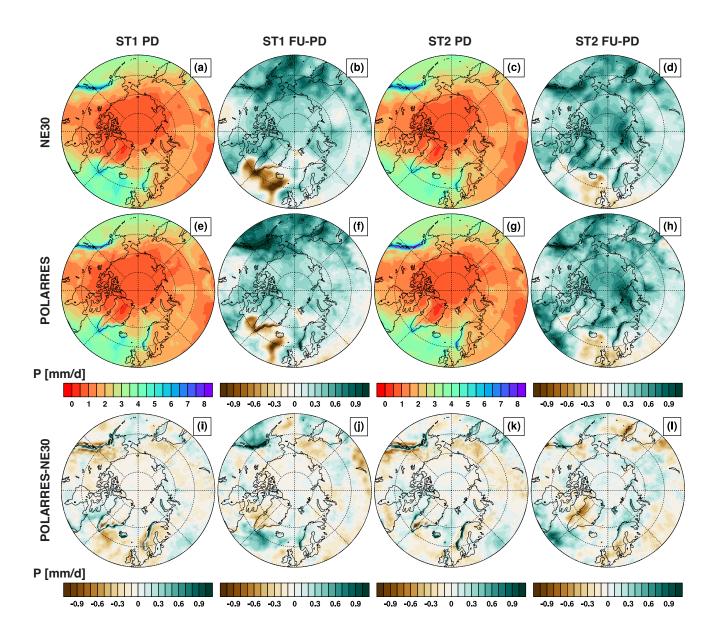
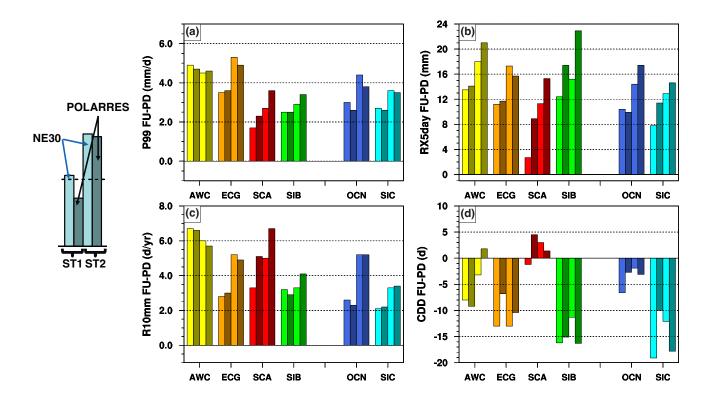


Figure 11. Same as Fig. 9, but for annual mean precipitation  $(mm d^{-1})$ 







**Figure 12.** Same as Fig. 10, but for the  $99^{th}$  percentile of daily precipitation (P99 (mm d<sup>-1</sup>); **a**), highest 5-day precipitation (RX5day (mm); **b**), heavy precipitation days (R10mm (dyr<sup>-1</sup>); **c**), and consecutive dry days (CDD (d); **d**)





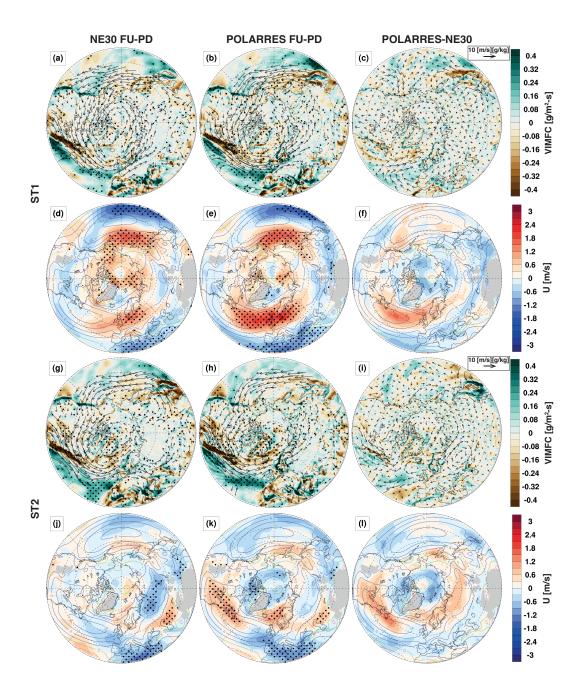


Figure 13. Projected future (2090–2099) changes in northern hemisphere (poleward of  $30^{\circ}$ N) vertically-integrated moisture flux convergence (VIMFC (g/m2 – s); shading) and 850 hPa moisture flux ((m/s)/ (g/kg); vectors) (a-c,g-i), and 850 hPa zonal wind (d-f,j-l; m/s; shading) as outputted by NE30 ( $1^{st}$  column) and POLARRES ( $2^{nd}$  column) for ST1 (a-f) and ST2 (g-l). The differences between NE30 and POLARRES are shown in the  $3^{rd}$  column. The zonal wind contours denote the climatological mean of the present-day zonal wind at 850 hPa, where red stands for positive (eastward) and blue stands for negative (westward). The dots and the vectors represent the significance of future changes at the 95% confidence level.





Table 1. Metrics of daily temperature and precipitation extremes used in this study

Index	Description
Temperature extremes	
TXx (°C)	Annual maximum of daily maximum temperature (TX)
TNx (°C)	Annual minimum of daily minimum temperature (TN)
WSDI $(\mathrm{d}\mathrm{yr}^{-1})$	Warm spell duration index, defined as the annual number of days in intervals of at least 6
	consecutive days where $TX > TX90$ , where $TX90$ is the $90^{th}$ percentile of daily maximum temperature, calculated for each calendar day using a running window of 15 days
$CSDI (dyr^{-1})$	Cold spell duration index, defined as the annual number of days in intervals of at least 6 consec-
	utive days where TN < TN10, where TN10 is the $10^{th}$ percentile of daily minimum temperature,
	calculated for each calendar day using a running window of 15 days
Precipitation extremes	
P99 $(\text{mm d}^{-1})$	99 <sup>th</sup> percentile of daily precipitation
RX5day (mm)	Highest amount of precipitation over an interval of 5 days
$R10mm~(\mathrm{d}\mathrm{yr}^{-1})$	Number of days with heavy precipitation, defined as daily precipitation that is equal to or higher than $10\mathrm{mm}\mathrm{d}^{-1}$
CDD (d)	Greatest number of consecutive days with daily precipitation less than $1\mathrm{mm}\mathrm{d}^{-1}$